Transportation Research Part B 44 (2010) 152–174

Contents lists available at ScienceDirect

Transportation Research Part B

journal homepage: www.elsevier.com/locate/trb

Development and calibration of the Anisotropic Mesoscopic Simulation model for uninterrupted flow facilities

Yi-Chang Chiu [a,*], Liang Zhou [b,1], Houbing Song [c,2]

[a] Department of Civil Engineering and Engineering Mechanics, The University of Arizona, 1209 E 2nd St., Tucson, AZ 85721, USA
[b] Wilbur Smith Associates, 2835 Brandywine Road, suite 400, Atlanta, GA 30341, USA
[c] Department of Electrical and Computer Engineering, The University of Virginia, 351 McCormick Rd., Charlottesville, VA 22904, USA

ARTICLE INFO

Article history:
Received 12 September 2008
Received in revised form 1 June 2009
Accepted 1 June 2009

Keywords:
Mesoscopic
Traffic simulation
Anisotropic
Dynamic traffic assignment
Speed Influencing Region

ABSTRACT

This paper presents the development, analysis, and calibration of the Anisotropic Mesoscopic Simulation (AMS) model for uninterrupted flow facilities, such as freeways. The proposed AMS model is a vehicle-based mesoscopic traffic simulation approach that explicitly considers the anisotropic property of traffic flow into the vehicle state update at each simulation step. The advantage of AMS is its ability to address a variety of uninterrupted flow conditions in a relatively simple, unified and computationally efficient manner.

The discussions focus on the key modeling concepts, the analytical properties and numerical analysis, and the calibration process and results. The addressed analytical properties are the overtaking conditions, acceleration and deceleration rate bounds, and shockwaves. The numerical analysis includes both freeway segments as well as merging junctions. Considerable efforts were devoted to employ the Next-Generation Simulation (NGSIM) program datasets to calibrate the AMS model parameters. The high traffic fidelity and satisfactory computational efficiency make AMS a promising simulation approach for large-scale regional dynamic traffic simulation and assignment.

1. Introduction

Traffic flow simulation models have been widely used for the purpose of analyzing transportation system performance because of their capability and flexibility to capture time-variant vehicular traffic dynamics. The levels of detail in these models range from microscopic, mesoscopic, to macroscopic. Macroscopic models depict the traffic at high levels of aggregation in flow, speed and density without having to explicitly represent vehicles. On the other hand, microscopic models are aimed at describing detailed information about an individual driver's adjustment of speed or lane position in reaction to other lead or adjacent vehicles, or roadway conditions. Generally, mesoscopic simulation models maintain varying degrees of characteristics associated with both macroscopic and/or microscopic models.

In the literature, several recent mesoscopic models have been developed; some have an explicit representation of individual vehicles that allows various decision rules vis-à-vis route, departure time and mode choices to be applied to individual motorists/vehicles. Such models were been developed as an integral part of simulation-based dynamic traffic assignment (SBDTA). Its macroscopic relation, which aims to maintain reasonable traffic flow dynamic, is utilized to evaluate the time-dependent link travel time and intersection turning penalties—solving the intermediate dynamic traffic assignment solutions during the solution process (Mahmassani et al., 1993; Ben-Akiva et al., 2001, 2003; Mahmassani, 2001; Taylor, 2003).

* Corresponding author. Tel.: +1 520 626 8462; fax: +1 435 921 1846.
E-mail addresses: chiu@email.arizona.edu (Y.-C. Chiu), lzhou@wilbursmith.com (L. Zhou), song@virginia.edu (H. Song).
[1] Tel.: +1 678 244 0278; fax: +1 770 936 8656.
[2] Tel.: +1 434 924 3960; fax: +1 434 924 881.

0191-2615/$ - see front matter © 2009 Elsevier Ltd. All rights reserved.
doi:10.1016/j.trb.2009.06.001

In the SBDTA model framework, the simulation model evaluates the intermediate assignment results and provides time-varying traffic statistics for the next-iteration assignment. Because SBDTA is aimed at regional modeling, the simulation model requires an algorithmic design that permits not only faster execution of simulation steps, but also more efficient computer memory usage in order to simulate millions or tens of millions of vehicles on a large network over a long time period in a computationally efficient manner. Application areas that favor such computational and algorithmic characteristics are generally imposed with large temporal and spatial scale modeling requirements, such as corridor traffic improvement and management, regional air quality analysis, or traffic modeling for mass evacuation.

It is generally agreed that using simulations to estimate the link travel time and intersection turning penalty exhibit several advantages over analytical approaches, such as BPR-type functions, because they lack realism in capturing the complex roadway–control–driver interactions (Peeta and Ziliaskopoulos, 2001; Ge and Carey, 2004). Nonetheless, the characteristics of various mesoscopic simulation models, such as the accuracy of their link travel times and intersection turning penalty estimation under various roadway conditions, have not been fully discussed and understood.

This paper presents the development, analysis, and calibration of the Anisotropic Mesoscopic Simulation (AMS) model for uninterrupted flow facilities, such as freeways. The proposed AMS model departs from prior models in that it is a vehicle-based mesoscopic traffic simulation approach that explicitly considers the anisotropic property of traffic flow into the vehicle state update at each simulation step. The discussions presented in this paper focus on the key AMS modeling concepts that include analytical properties and numerical analysis, and the calibration process and results. The overtaking conditions, acceleration and deceleration rate bounds, and shockwaves are the addressed analytical properties. The numerical analysis includes both freeway segments and merging junctions. Considerable efforts were devoted to employing the Next-Generation Simulation (NGSIM) program datasets to calibrate the AMS model parameters.

The methodological contribution of this research is in the theoretical development of the innovative modeling approach and polynomial algorithmic procedure, analytical and numerical analysis of various intuitive and desirable traffic properties, and the carryout of a validation and calibration of AMS using actual field data.

The study described in this paper is a part of a larger study. The discussions in this paper are limited to uninterrupted flow facilities. Applying AMS to interrupted facilities requires a careful examination of intersection signals and queue formation for different turning movements, as well as calibration; therefore, these issues are not addressed in this paper.

This paper is presented according to the following structure: Section 2 reviews the existing related traffic simulation models; Section 3 introduces the Anisotropic Mesoscopic Simulation (AMS); Section 4 discusses the analytical properties of the AMS model, including the non-overtaking conditions and acceleration and deceleration bounds and shockwaves; Section 5 presents a set of numerical results for both non-homogeneous freeways and merging junctions; Discussed in Section 6 are the calibration results using the NGSIM data. Lastly, Section 7 offers concluding remarks and discusses further research ideas.

2. Literature review

In the literature, the definitions and development focus of mesoscopic traffic flow models vary widely, and several different models with distinct modeling concepts can be found. Earlier models include the headway distribution model that assumes probability distribution functions to capture vehicle traffic dynamics (Buckley, 1968; Branston, 1976); the cluster model (Botma, 1978); the gas-kinetic continuum model, first published by Prigogine and Herman, which employs the Phase-Space Density (PSD) as its core mechanism (Nelson and Sopasakis, 1998).

Another model class is the simulation-oriented models that are aimed at describing vehicle trajectories following link, segment, or cell structure of the network arcs at every simulation clock tick. Falling within this category are several other types of models with distinct modeling features. A common model type is the link-based queue-server models. The Queue model introduced by Gawron (1998) describes the links with a flow capacity that limits the number of agents that can leave the link and a space constraint which defines the limit of the number of agents that can be on a link at the same time. The spillback modeling issue appeared in the original model (Gawron, 1998) was later addressed by Cetin et al. (2003).

In another type of model in the same category, vehicles are moved according to an average speed calculated from the average link density in conjunction with a macroscopic speed–density (v–k) relationship at every clock tick. A queue-server at the downstream node discharges vehicles according to the constraints imposed at these nodes, accounting for delays caused by traffic signals, downstream capacity limits, and interaction with additional traffic. A typical model requires a non-zero minimal speed to prevent a complete stop once the link density reaches the jam density. A vehicle's change of speed when moving from one upstream link to the downstream link is not explicitly regulated. A typical model is DYNASMART (Jayakrishnan et al., 1994).

Improved versions of this model are the DynaMIT DTA model (Ben-Akiva et al., 1998) and MEZZO (Burghout, 2004), in which a link is divided into two segments with one consisting moving vehicles and the other with possible queued vehicles. All moving vehicles move at the same speed, which is calculated using a method similar to that in DYNASMART. If no queue exists, the speed transition from one link to its downstream link is considered. This is based on the assumption that speed is constant on the upstream section of the link, followed by a deceleration zone covering a downstream section, where the speed of vehicles varies linearly as a function of the position. The length of the deceleration zone depends on the geometry

of the segment and traffic conditions. In the case of a queue, the queue segment contains queue vehicles with separate simulation logics to handle queue formation and dissipation.

In CONTRAM (Leonard et al., 1989; Taylor, 2003), vehicles within the links are grouped into packets and each packet is treated as one vehicle. The packets are arranged in order of their entry time and the travel time is calculated, assuming that packets experience junction delays as a function of current flow on the link. Vehicles entering or leaving the link are respectively added or subtracted in the appropriate time intervals to produce new flow estimates.

A similar concept, called the *space–time queue* (STQ), was proposed by Mahut (Mahut, 2001; Mahut et al., 2002). The network loading problem is solved using a traffic simulation model that moves individual vehicles according to the triangular flow–density relationship. In the case of a one-lane link, the model is the discrete-flow equivalent of the simplified kinematic wave model of Newell (Newell, 1993; Mahut, 2001). Rather than computing a real-valued amount of flow that can pass a point (node) over a fixed time interval (as in Newell's model), this model calculates the real-valued duration of time that separates fixed-size increments of flow (individual vehicles) at a given point, similar to the discrete-event simulation concept. This model was later implemented as part of the DTA model DYNAMEQ (Mahut et al., 2004; INRO, 2005).

A recent study (Dell'Orco, 2006; Celikoglu and Dell'Orco, 2007) categorized dynamic disaggregate mesoscopic network loading problems based on whether vehicles are either grouped into discrete packets or spread within continuous packets. Continuous packets mean that vehicles are distributed inside each packet, which is defined by the head and the tail points; and discrete packets mean that all vehicles belonging to a packet are grouped and represented by a single point. In the same studies, a model with uniformly accelerated discrete packets was proposed. However, this model also assumed that the speeds of all vehicles on the same link are determined by all vehicles on that link.

A common problem arising in existing mesoscopic algorithms, as pointed out by (Dell'Orco, 2006), is representing the anisotropic traffic flow property because all moving vehicles move at the same speed based on the link average density; in the case of a long link, the leading moving vehicles' speed will be affected by the inflow of the link, implying that a infinite-speed forward moving shockwave is always generated during simulation. This violates the basic anisotropic property of traffic flows, which says that vehicles mostly react to other vehicles that are in front of them as also pointed out in some earlier articles (Daganzo, 1995a,b; Zhang, 2001) although these discussions focus more on the higher-order continuum models. Not observing the anisotropic property can underestimate the recovery of traffic congestion. This is a result of the leading vehicles moving at unrealistically slow speeds regardless of the capacity restoration downstream from the link.

Handling the queue formation and discharge processes in the queue-server type of models is particularly challenging. Some models either use a virtual queue in conjunction with minimal positive speed (Jayakrishnan et al., 1994) or explicitly capture the queue dynamics but with a family of different models that work in a rather ad hoc manner (Ben-Akiva et al., 1998). Because the virtual queue does not correspond to actual traffic characteristics, these models may not necessarily capture traffic dynamic characteristics (e.g. queue lengths, delays, shockwaves, etc.).

Ben-Akiva et al. (Ben-Akiva et al., 1998; Ben-Akiva, 2003a,b) and Burghout (Burghout, 2004) attempted to improve queue modeling. The proposed technique is to treat moving and queued segments of a link separately while vehicles in the free-moving portion of the link move according to a user-defined macroscopic v–k relationship. In the event that a queue is identified, a family of different deterministic models is used to approximate the queue formation or dissipation processes (Ben-Akiva et al., 1998, 2003). Such an approach may only be suitable for arterial streets, in which queues are constantly formed by traffic signals. For uninterrupted flow facilities, such as freeways, defining distinct free-moving and queued portions of the traffic stream in general traffic conditions may be difficult. Transient queues or shockwaves caused by temporary flow state transitions may not be detected unless more complex rules are devised.

The Cell Transmission Model (CTM) proposed by Daganzo (Daganzo, 1994; Daganzo, 1995a,b) is an approximation of the Lighthill and Whitham's (Lighthill and Whitham, 1955) and Richards' (Richards, 1956) equations by a set of difference equations. Specifically, a link is divided into homogeneous cells according to the free-flow speed of that link, which are numbered consecutively from upstream of the link. The cell transmission determines the flow at a certain point of a road according to the downstream and upstream cell flow situation. The cell size can be sufficiently small to capture the state of individual vehicles while reasonably capturing both free-flow conditions as well as interrupted flows. CTM's applicable range has been extended from uninterrupted to generalized interrupted flow conditions (Ziliaskopoulos and Lee, 1997). CTM has also been used as a network loading model to support SBDTA (Boyles et al., 2005). In addition, it has also been formulated as a mathematical problem to solve an array of network flow problems (Li et al., 1999; Waller et al., 2001; Ziliaskopoulos and Waller, 2001; Ge and Carey, 2004; Chiu and Zheng, 2007; Chiu et al., 2007).

3. Anisotropic Mesoscopic Simulation modeling concept and basic properties

The AMS model is developed based on two intuitive concepts and traffic characteristics: (1) at any time, a vehicle's prevailing speed is influenced only by the vehicles in front of it, including those that are in the same or adjacent lanes and (2) the influence of traffic downstream upon a vehicle decreases with increased distance. These two characteristics define the

"anisotropic" property of the traffic flow and provide the guiding principle for AMS model design. Based on such concepts, we define that for any vehicle *i*, only those leading vehicles (in the same lane or in the adjacent lanes) present in vehicle *i*'s immediate downstream and within a certain distance are considered to influence vehicle *i*'s speed response. This is a similar concept to a stimulus–response type of car-following model, with the distinction that in AMS, the stimulus of a vehicle's speed response is represented in a macroscopic manner instead of using inter-vehicle distance or speed as in microscopic models.

For modeling purposes, the Speed Influencing Region (*SIR*) for vehicle *i* is defined as vehicle *i*'s immediate downstream roadway section in which the stimulus is significant enough to influence vehicle *i*'s speed response. This concept is further depicted in Fig. 1, in which a multi-lane homogeneous roadway segment is considered. The Speed Influencing Region (*SIR*) for vehicle *i* is defined as the area (including the lane in which vehicles reside and all the adjacent lanes) in front of vehicle *i*, where the traffic condition (represented by the density) affects vehicle *i*'s speed response. At each simulation clock tick, vehicle *i*'s speed is influenced by the density in *SIR*. The upstream traffic and downstream traffic outside the *SIR* does not influence vehicle *i*. The SIR_i length can be assumed to be either equal for all vehicles or variable according to different flow conditions. The SIR_i length is assumed to be an average value l across all vehicles in this paper. The traffic density in SIR_i, denoted as k_i, is calculated as the number of vehicles present in SIR_i divided by the total lane-miles of the SIR_i. As such, the unit of k_i becomes the number of vehicles per mile per lane.

At the beginning of a simulation interval, for each vehicle *i*, the prevailing speed of vehicle *i* during the simulation interval is determined by Eq. (1), where $\wp: k \to v$ is a non-increasing speed–density relationship function with two boundary conditions: $\wp(0) = v_f$ and $\wp(k_{jam}) = 0$.

The algorithmic steps of an AMS model during simulation are as follows: at each clock tick t (the beginning of a simulation interval), each vehicle's speed v_i^t is evaluated based on its *SIR* density, which is obtained from the previous clock tick k_i^{t-1} through the v–k relationship function $\wp(k_i^{t-1})$. The *SIR* density is calculated based on Eqs. (2) and (3), depending on whether or not the *SIR* spans over the freeway segment with a different capacity. If the *SIR* spans a homogeneous highway section, Eq. (2) applies; otherwise, Eq. (3) is used. Vehicle *i*'s traveling distance at the end of the current simulation interval is obtained by taking the prevailing speed v_i^t times the duration of the simulation interval Δ.

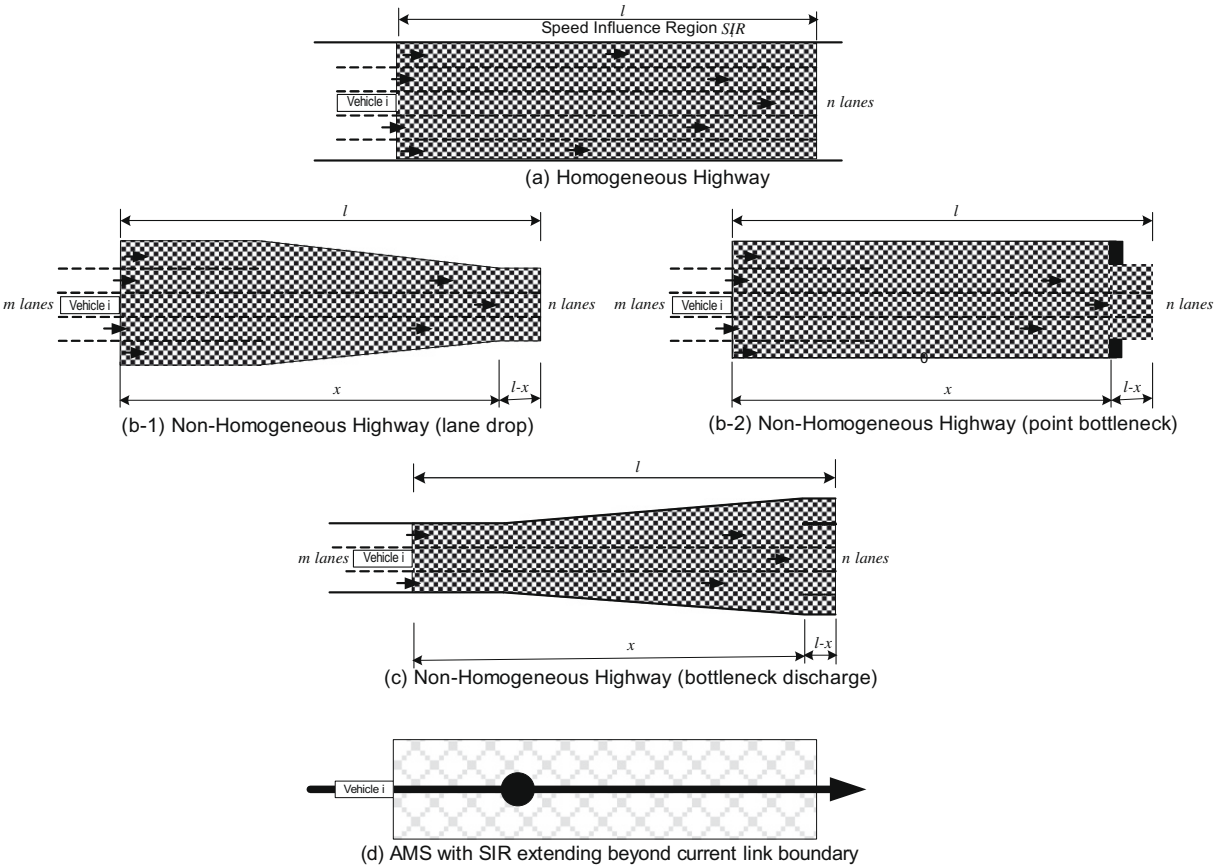

Fig. 1. AMS model concept.

$$v_i^t = \wp\left(k_i^{t-1}\right) \tag{1}$$

$$k_i^{t-1} = \min\left[k_{jam}, \frac{N_i^{t-1}}{nl}\right] \tag{2}$$

$$k_i^{t-1} = \min\left[k_{jam}, \frac{N_i^{t-1}}{mx_i^{t-1} + n(l - x_i^{t-1})}\right] \tag{3}$$

where i is the subscript denoting a vehicle. The index i decreases with vehicles traveling in the same direction on the same link, t the superscript denoting a simulation interval, l the *SIR* length, x_i^{t-1} the distance between vehicle i and the upstream edge of lane drop (open) or the location of point bottleneck within *SIR* at clock tick $t-1$, m the number of lanes for the *SIR* area designated with x_i^{t-1}, n the number of lanes for the *SIR* area outside that is designated with x_i^{t-1}, v_i^t is the prevailing speed of vehicle i during simulation interval t, k_i^{t-1} the density of the *SIR* for vehicle i, N_i^{t-1} the number of vehicles present in *SIR*, excluding vehicle i, v_f the free-flow speed in the speed–density relationship, $\wp : k \to v$ the non-increasing speed–density function specifying the v–k relationship, where $\wp(0) = v_f$ and $\wp(k_{jam}) = 0$, k_{jam} the jam density, and $\wp(k_{jam}) = 0$.

During the AMS simulation, each vehicle maintains its own prevailing speed and *SIR* at the beginning of a simulation interval. Individual vehicles' traveling distances are therefore likely to differ, even though they are on the same link. This feature is different from certain previous models (Jayakrishnan et al., 1994; Balakrishna et al., 2005), in which all moving vehicles on the same link travel at the same speed. This characterizes the AMS model as a vehicle-based mesoscopic model having a greater degree of resemblance with car-following-based microscopic models. The major difference between AMS and car-following models is that in AMS, a vehicle's speed adjustment at each simulation time interval is governed by the *SIR* density k_i^t, which is a macroscopic measure of all the vehicles present in the *SIR* region, instead of an inter-vehicle measure between the target and the leading vehicle(s).

Since the *SIR* moves with each vehicle during simulation, it can be anticipated that in the AMS model, the vehicle advancing mechanism is generally independent of the representation of network structures (i.e. size/length of cell/segment/link) under the uninterrupted flow condition. Each vehicle makes speed adjustment decisions solely based on its *SIR* density; the AMS simulation results generally remain stable regardless of how link lengths are defined unless the link is shorter than a certain threshold that violates that required by a general time-based simulation.

AMS handles queue formation/discharge in a natural and straightforward manner. When k_{jam} is reached, $v = \wp(k_{jam}) = 0$; vehicles speed up when the *SIR* density decreases. This mechanism allows for clear representations of substantial or transient queue formation or discharge. When a free-moving vehicle approaches the end of a queue, its speed gradually approaches the same speed of the queue tail as its *SIR* density approaches the *SIR* density of the leading vehicles. Depending on how the overtaking condition is met, this vehicle may trail at the end of the queue without "jumping over" leading vehicles, or it may stop ahead of the leading vehicle. More explanations in this regard are offered in Section 4.1.

Eq. (1) was further extended to simulate traffic flow in uninterrupted flow facilities under various configurations, such as homogeneous highways, non-homogeneous highways (e.g. lane drops, bottleneck discharge, or merging/diverging) and temporary blockage, by specifically considering different *SIR* density k_i^t calculations corresponding to those conditions. As shown Eq. (2), in the case of the homogeneous highway, k_i^t is calculated as the number of vehicles presenting in the *SIR* divided by the total lane-miles of the *SIR* (i.e. the *SIR* length times the number of lanes). When lane drops or lane additions occur within the *SIR*, the total lane-mile of *SIR* is the sum of lane-miles of separate sections, as shown in Eq. (3). When the lane drop (Fig. 1b-1) or point bottleneck (Fig. 1b-2) (from m to n lanes, $n < m$) occurs downstream from vehicle i within the *SIR* range, the total lane-miles in the *SIR* is calculated as $mx + n(l - x)$, and the resulting k_i^t is the smaller of k_{jam} and $\frac{N_i^{t-1}}{mx+n(l-x)}$, which is the number of vehicles in the *SIR* at the beginning of the time interval $t-1$ divided by the total lane-miles $mx + n(l - x)$ in the *SIR*.

In the case of a lane drop or a point bottleneck ($n < m$), the *SIR* density of a vehicle gradually increases (and hence speed reduces) as it approaches the bottleneck. When $n = 0$, a complete blockage occurs; this can be applied to either a point blockage or a red-light signal indication situation. On the other hand, in the case of discharging from a bottleneck, as a vehicle approaching the open-up of the bottleneck, the density reduces and speed increases gradually.

To ensure desirable computation tractability of AMS, the following polynomial algorithmic procedure is proposed. At each simulation clock tick, Step *VS* updates individual vehicle speeds. In Step *VS.1*, for each link h, vehicles are scanned and updated only once from the tail to the head of the data structure holding the vehicle IDs. The complexity of Step *VS* is $O(z)$, where z is the total number of vehicles present in the simulation at clock tick t. With the updated vehicle speed v_i^t, Step *VP* updates the position of all vehicles according to the prevailing speed v_i^t. The complexity of Step *VP* is also generally $O(z)$ if non-overtaking is observed.

For those links with incoming vehicles, Step *VR* updates its vehicle list. The complexity of this step is $O(z)$ because these incoming vehicles are typically appended to the end of list without insertion. Step *VA* updates individual vehicles' *SIR* density k_i^t after all the vehicles are updated with a new position. k_i^t will be used for the Step *VS* in next simulation instant $t+1$. The key of this algorithmic step is, for those vehicles whose *SIR* front remains in the same link, to update the increment of density when scanning from vehicle $i-1$ to vehicle i without re-counting the number of vehicles in *SIR* for vehicle i. This allows the complexity of Step *VA* to be $O(z)$. The algorithm comprising four updating steps is briefly presented as follows.

Given: for $h \in \{all\ links\}$, vehicles present at each link are stored in a data structure Q_h in ascending order of their distance to the downstream node at the beginning of the simulation interval t.

1. (Step *VS*) Vehicle speed update:
   (Step *VS.1*) For link $h \in \{all\ links\}$, do the following,
   (Step *VS.1.1*) For vehicle $i \in Q_h$, do the following,
   Retrieve k_i^{t-1} from computer memory,
   Calculate $v_i^t = \wp(k_i^{t-1})$.
2. (Step *VP*) Vehicle position update:
   (Step *VP.1*) For $h \in \{all\ links\}$, do the following,
   (Step *VP.1.1*) For vehicle $i \in Q_h$, do the following,
   (Step *VP.1.1.1*) Read v_i^t and y_i^{t-1} from computer memory and update vehicle i's position to be $y_i^t = y_i^{t-1} - v_i^t \cdot \Delta$, where Δ is the simulation interval.
   (Step *VP.1.1.2*) if $y_i^t < 0$, mark η_i vehicle i's arrival time at the downstream end. Retrieve vehicle i's next traversing link ID b, insert vehicle i to the incoming vehicle list ψ_b in the ascending order of downstream end arrival time. Increase the incoming vehicle counter $\theta_b \leftarrow \theta_b + 1$.
   (Step *VP.1.2*) Update vehicle i's order in h based on y_i^t.
3. (Step *VR*) Vehicle relocation:
   (Step *VR.1*) For $h \in \{all\ links\}$, retrieve ρ_h the allowed max number of incoming vehicles for link h[a] for Δ, do the following,
   (Step *VR.1.1*) For the first $g = \min\{\rho_h, \theta_h\}$ vehicles in ψ_h, do the following,
   (Step *VR.1.1.1*) Insert $i \in \psi_h$ into Q_h. Delete vehicle i from their respective Q.
   (Step *VR.1.1.2*) Update vehicle i position on link h as $y_i^t = \lambda_h - v_i^t \cdot (\Delta - \eta_i)$
4. (Step *VA*) AMS variable update:
   (Step *VA.1*) For link $h \in \{all\ links\}$, do the following,
   (Step *VA.1.1*) For vehicle $i \in Q_h$, do the following,
   (Step *VA.1.1.1*) Calculate N_i^t based on the following conditions:
   Calculate the position of the *SIR* front for vehicle i to be $s_i^t = y_i^t - l$.
   If (vehicle i is the farthest from the downstream node) then
   If $(s_i^t \geq 0)$ then,
   Calculate N_i^t as the number of vehicles i: $s_i^t \leq y_{k\neq i}^t < y_i^t$.
   Else,
   Find vehicle i's next traversing link ID b and its length λ_b. Calculate N_i^t as the sum of the number of vehicles $i \in Q_h$: $0 \leq y_{k\neq i}^t < y_i^t$ and the number of vehicles $k \in Q_b$: $\lambda_b - (l - y_i^t) \leq y_k^t$.
   else,
   If $(s_i^t \geq 0)$ then,
   Calculate $N_i^t = N_{i-1}^t - 1 + \widehat{N}_i^t$, where $\widehat{N}_i^t$ is the number of vehicles located between s_{i-1}^t and s_i^t,
   $s_i^t = s_{i-1}^t - (y_{i-1}^t - y_i^t)$, where $(y_{i-1}^t - y_i^t)$ is the distance between vehicles i and $i-1$.
   Else,
   Find vehicle i's next traversing link ID b and its length λ_b. Calculate $\widehat{N}_i^t$ as the sum of the number of vehicles $i \in Q_h$: $0 \leqslant y_{k\neq i}^t < y_i^t$ and the number of vehicles $k \in Q_b$: $\lambda_b - (l - y_i^t) \leq y_k^t$
   (Step *VA.1.1.2*) Calculate k_i^t using Eqs. (2) or (3).

[a] This is calculated by other capacity update modules and is not discussed in details herein.

4. Analytical properties

Based on the above algorithmic procedure, certain microscopic and macroscopic properties for AMS can be understood analytically. This section discusses the microscopic properties related to vehicle overtaking, deceleration/acceleration and overtaking, as well as macroscopic properties related to shockwaves.

4.1. Microscopic properties

4.1.1. Overtaking conditions

Overtaking is defined as the situation in which $y_{i-1}^{t-1} \geq y_i^{t-1}$ and $y_{i-1}^t \leq y_i^t$, where y_i^t is the position of vehicle i at time t and y_{i-1}^t is the position of the following vehicle $i-1$ at time t. This occurrence is a likely scenario in AMS because each vehicle's prevailing speed is calculated individually. For any two consecutive vehicles, $i-1$ and i, given a predetermined *SIR* length l, jam density k_{jam}, and simulation interval Δ, Lemma 1 holds. Lemma 1 indicates the condition in which vehicle $i-1$'s speed is greater or equal to vehicle i. $v_{i-1}^t \geq v_i^t$ is the necessary condition for the overtaking to occur at time t.

Notations	
l	length of *SIR*, assume to be the same for all vehicles
v	vehicle speed
k	*SIR* density
Δ	duration of a simulation interval
$\wp : k \to v$	non-increasing function specifying the v–k relationship, $\wp(0) = v_f$ and $\wp(k_{jam}) = 0$
k_{jam}	jam density

Lemma 1

On a homogeneous highway section, at clock tick t, $v_{i-1}^t > v_i^t$ if and only if there are at least two vehicles present between the front end of the Speed Influencing Regions (*SIR*s) of vehicles $i-1$ and i. (4)

Proof (*See Appendix B*).

Theorem 1 (Non-overtaking Sufficient Conditions). *In the AMS model, given the speed–density function $\wp : k \to v$, if the following conditions are satisfied, then no vehicle overtaking will occur during simulation:*

1. Speed—density function $\wp : k \to v$ is non-increasing, and (5)
2. The length of the Speed Influencing Region (*SIR*) $l > -\min(\wp') \cdot \Delta \cdot k_{jam}$ (6)

The proof for Theorem 1 is provided in Appendix C.

Theorem 1 is a sufficient condition that prevents overtaking from occurring during simulation. For illustration purposes, we discuss the non-overtaking conditions using Greenshield's type of speed–density function with the form of $v = v_f(1 - k/k_{jam})^{\alpha}$. The first-order derivative of the function leads to $\wp' = \alpha v_f(1 - k/k_{jam})^{\alpha-1} \cdot (-1/k_{jam})$. Examining the second-order derivative, one can find that $\wp'' = \alpha(\alpha-1)v_f(1 - k/k_{jam})^{a-2} \cdot (1/(k_{jam})^2)$ if $\alpha \geqslant 1$. For most of the model forms found in literature, $\alpha = 1$ leads to Greenshield's model and $\alpha > 1$ is found in most field data (Mahmassani et al., 2003; Ben-Akiva et al., 2004; Balakrishna, 2006). To this extent, $k = 0 = \arg\min(\wp')$, $\wp'(0) = \alpha v_f \cdot (-1/k_{jam})$ and $\wp'(k_{jam}) = 0$. With $\min(\wp') = \wp'(0) = \alpha v_f \cdot (-1/k_{jam})$, we have $\alpha v_f \cdot \Delta \leq l$. As an example, for a highway section with 50 mph free-flow speed and a simulation interval of 3 s, the *SIR* length needs to be greater than or equal to 220α ft to prevent overtaking. Note that $\alpha = 1$ refers to Greenshield's model; some calibrated models have α ranging from 2.0 to 5.5 (Mahmassani et al., 2003), resulting in *SIR* lengths of 440–1100 ft.

Theorem 2 (Overtaking sufficient conditions). *In the Anisotropic Mesoscopic Simulation model, given the speed–density function $\wp : k \to v$, if the following conditions are satisfied, then vehicles $i-1$ will overtake vehicle i at clock tick t:*

1. Speed—density function $\wp : k \to v$ is non-increasing, and (7)
2. The spacing between vehicles $i-1$ and i is less or equal to the *SIR* length l, and (8)
3. The *SIR* length $l < \Delta \cdot k_{jam} \cdot \dfrac{\wp(k_{i-1}^t) - \wp(k_i^t)}{k_{jam} - k_{i-1}^t}$ (9)

The proof for Theorem 2 is presented in Appendix D.

Theorem 2 indicates that the vehicle overtaking occurrence is jointly determined by model parameters as well as the relationship between vehicles $i-1$ and i at clock tick t as depicted by Eqs. (1)–(3). Overtaking is illustrated through an example in which vehicle $i-1$ travels at free-flow speed v_f, i.e. $k_{i-1}^t = 0$, whereas vehicle i stops at the tail of a standing-still queue, i.e. $k_i^t = k_{jam}$. Assuming a 3-s simulation interval, if $l < \Delta \cdot k_{jam} \cdot \frac{v_f}{k_{jam}} = \Delta \cdot v_f = 3 \cdot 73.3 = 220$ ft and the spacing between vehicles $i-1$ and i at the clock tick t is less or equal to l, then vehicle $i-1$ overtakes vehicle i after the position update at clock tick t.

4.1.2. Bounds for deceleration and acceleration rates

Acceleration and deceleration rates are defined as a vehicle's speed change from time $t-1$ to t, divided by the simulation interval. Acceleration/deceleration rates are of particular interest when considering using them to support certain modeling applications, such as local level air quality analysis, in which vehicle acceleration/deceleration rates are inputs for the air quality model.

Theorem 3 (Deceleration bound). *If $v_{i-1}^t < v_{i-1}^{t-1}$ then the deceleration rate of vehicle $i-1$ at time t during simulation is within the following bound:*

$$0 \geq a_{i-1}^{t} \geq \wp'(k_{i-1}^{t-1})\lambda + \frac{\wp''(k_{i-1}^{t-1})}{2!}\lambda^2\Delta + \frac{\wp'''(k_{i-1}^{t-1})}{3!}\lambda^3\Delta^2 + \cdots,$$
$$\text{where } \lambda = \frac{[\wp(k_{i-1}^{t-1}) - \wp(k_i^{t-1})]\cdot k_{jam}}{l} > 0 \tag{10}$$

Theorem 4 (Acceleration bound). *If $v_{i-1}^{t} > v_{i-1}^{t-1}$, then the acceleration rate of vehicle $i-1$ at time t during simulation is within the following bound:*

$$0 \leq a_{i-1}^{t} \leq \wp'(k_{i-1}^{t-1})\lambda + \frac{\wp''(k_{i-1}^{t-1})}{2!}\lambda^2\Delta + \frac{\wp'''(k_{i-1}^{t-1})}{3!}\lambda^3\Delta^2 + \cdots,$$
$$\text{where } \lambda = \frac{[\wp(k_{i-1}^{t-1}) - \wp(k_i^{t-1})]\cdot k_{jam}}{l} < 0 \tag{11}$$

Theorems 3 and 4 indicate that vehicle $i-1$'s deceleration/acceleration rate is jointly determined by the relative speed between vehicle $i-1$ and its leading vehicle i (through λ), as well as the speed of vehicle $i-1$ at time $t-1$ (through $\wp'(k_{i-1}^{t-1}), \wp''(k_{i-1}^{t-1}), \wp'''(k_{i-1}^{t-1}), \ldots$.), and the simulation interval Δ. It is trivial to show that when $v_{i-1}^{t} = v_{i-1}^{t-1}$, $\lambda = 0$, and $a_{i-1}^{t} = 0$. The mathematical derivations of Theorems 3 and 4 are presented in Appendix E.

It can be seen from Theorems 3 and 4 that when $\wp(k_{i-1}^{t-1}) = \wp(k_i^{t-1})$, $\lambda = 0$, and $a_{i-1}^{t} = 0$, and $\wp(k_{i-1}^{t-1}) > \wp(k_i^{t-1})$, $\lambda > 0$, deceleration occurs. Likewise, acceleration occurs when $\wp(k_{i-1}^{t-1}) < \wp(k_i^{t-1})$.

The acceleration rates based on varying speeds of vehicles $i-1$ and i are displayed in Figs. 2 and 3. In Fig. 2, it appears that $a_{i-1}^{t} = 0\ \forall\ \wp(k_{i-1}^{t-1}) < \wp(k_i^{t-1})$. The deceleration rate increases with increasing vehicle $i-1$ speed and with increasing speed difference between vehicles $i-1$ and i. The maximal deceleration rate occurs at around -12.2 f/s^2 when vehicle $i-1$'s speed is at the free-flow speed and vehicle i's speed is lower than 16.7 mph.

Following Theorem 4, acceleration occurs when $\wp(k_{i-1}^{t-1}) < \wp(k_i^{t-1})$. Using the same example, the maximal acceleration was found to be about 11.5 f/s^2, and it occurs when vehicle i is at the free-flow speed and vehicle $i-1$ is at a speed lower than 5.0 mph. When vehicle i is at a lower speed, the acceleration rate for vehicle $i-1$ is capped at a lower rate. In other words, when vehicle i's speed is much higher that that of vehicle $i-1$, vehicle $i-1$ will accelerate at a higher rate to keep up with the speed of vehicle i as soon as possible. Also note that if overtaking does not occur, then vehicle $i-1$'s acceleration will stop once it reaches vehicle i's speed.

In the illustrated examples, both the deceleration and acceleration rates yielded by AMS simulation are within a comparable range and pattern with real-world observations as well as prevalent microscopic simulation models such as CORSIM (FHWA, 2007) and VISSIM (PTV, 2009).

4.2. Macroscopic properties – shockwaves

The shockwaves caused by highway capacity (e.g. lane drop or expansion, or incidents) can be estimated by macroscopic approaches using q–k fundamental diagrams. In AMS, vehicles will slow down due to the same conditions and such changes

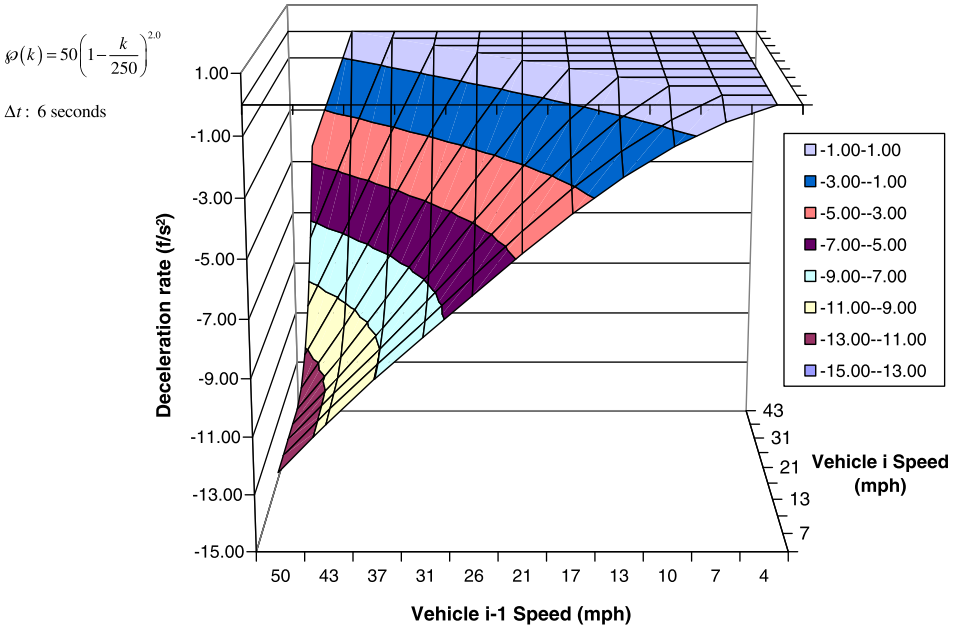

Fig. 2. Vehicle deceleration conditions.

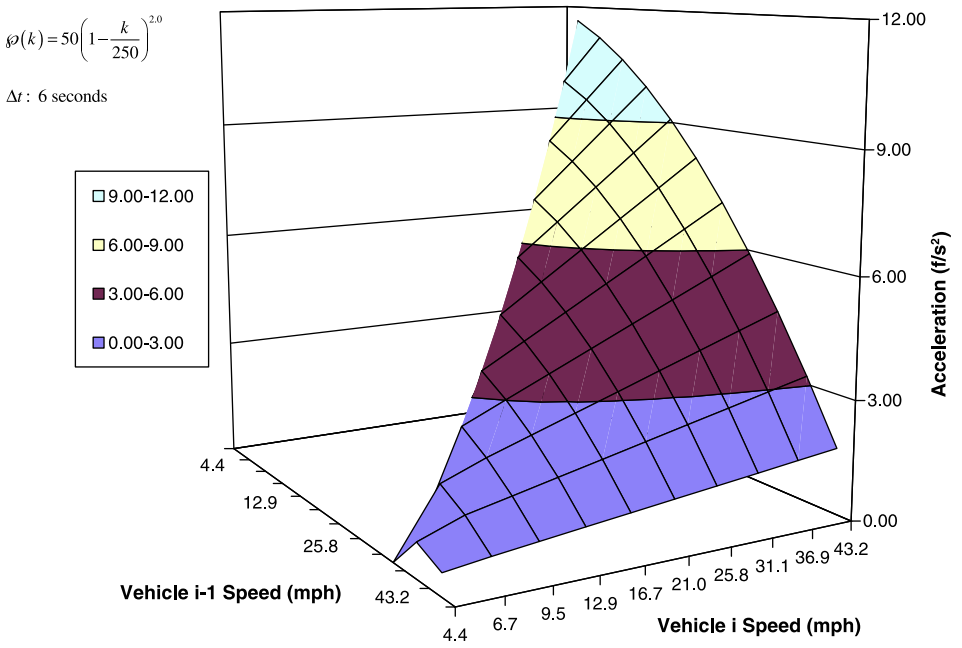

Fig. 3. AMS vehicle acceleration conditions.

of traffic flow will also cause shockwaves to form. Theorem 4 indicates that the shockwaves generated by AMS are identical to those estimated by the macroscopic q–k diagram based approach under the specified model setting.

Theorem 4 (AMS Shockwave Speed). *Given the AMS settings (12) and (13), the speed of the backward shockwave generated by AMS simulation of vehicles approaching the tail of a standing-still queue equals to that calculated by* $\omega_{ab} = \frac{q_a - q_b}{k_a - k_b}$ *using the q–k diagram:*

$$l = v_f \cdot \Delta \tag{12}$$

$$v = v_f\left(1 - \frac{k}{k_{jam}}\right) \tag{13}$$

Proof (*see Appendix F*).
The above discussion depicts AMS' general analytical properties that aid in understanding certain key microscopic and macroscopic traffic simulation characteristics. However, numerical examples are also needed to provide insights regarding the actual numerical simulation outcomes. In the next section, the numerical properties of the AMS model are illustrated and discussed through two freeway simulation cases, including a non-homogeneous freeway segment and a freeway merging junction. □

5. Numerical analysis

5.1. Simulation of a non-homogeneous highway segment

This simulation experiment was conducted on a one-way, two lane, 60-mile-long freeway segment with a permanent lane drop and a temporarily roadway blockage. The permanent lane drop is located between the 30 and 40 mile posts. The temporary roadway blockage, closing the entire roadway from 100 to 200 min after the simulation start, is located 10 miles downstream from the permanent lane drop (see Fig. 4). Constant vehicle loading is set at 1500 passenger-car per-hour per-lane (pcphpl), which leads to a total of 12,000 vehicles to be generated during a 240-min simulation period. Simulation intervals are set to be 6 s. The trajectories of sample vehicles are recorded at clock tick in order to construct detailed space–time diagrams. The two-regime modified Greenshield's model without a minimal positive speed $\wp(k) = v_f,\ \forall\ k \leqslant 30; \wp(k) = 77.9(1 - k/200)^{2.73},\ \forall\ 30 \leqslant k \leqslant 200$ is used in the experiment. The *SIR* length l is set to be 1000 ft with a simulation interval of 6 s, and free-flow speeds for all highway segments are set to 48 mph.

Fig. 5a illustrates the chosen $\wp(k)$ function, while Fig. 5b is the q–k relationship that is mathematically equivalent to $\wp(k)$. Fig. 5c shows all the speed–density data points collected from the simulation. The comparison between Fig. 5b and c

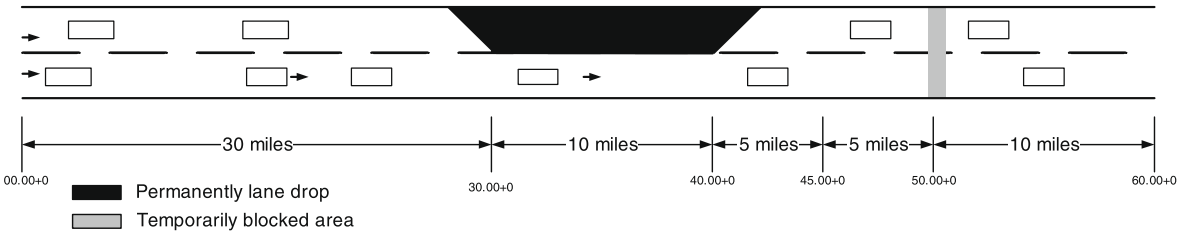

Fig. 4. Test network for AMS model (not to exact scale).

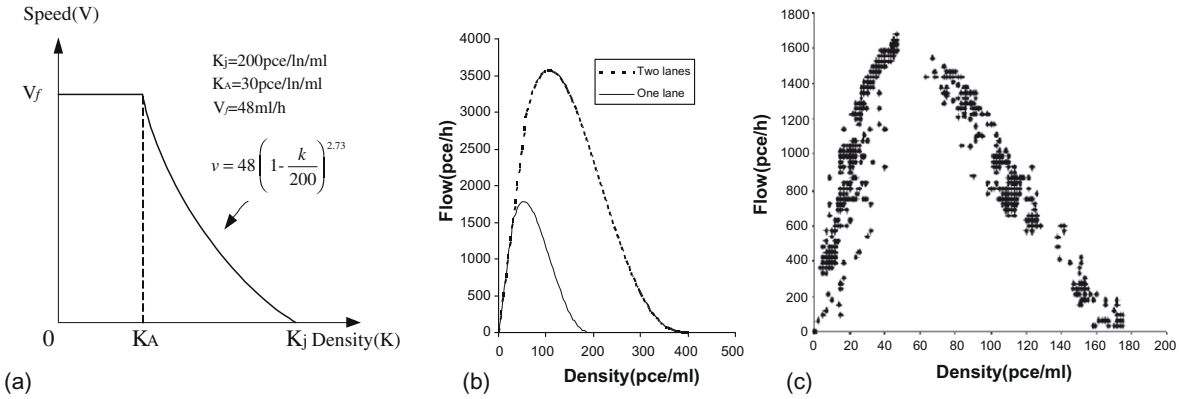

Fig. 5. (a) Modified Greenshield's model used in AMS, (b) theoretical equivalent q–k diagram, and (c) q–k data collected from the AMS model.

indicates that the q–k relation represented by the AMS model closely matches the theoretical patterns. The resemblance reiterates that the AMS model exhibits consistent and intuitive macroscopic characteristics.

The space–time plots for a set of sample vehicles are illustrated in Fig. 6. Vehicles initially travel at a free-flow speed (48.0 mph) before they reach the lane drop. Upon entering the lane drop section, the density increases and speed drops to approximately 17.2 mph. Upon exiting the lane drop section, vehicles accelerate to the speed corresponding to the saturation flow rate. Those vehicles which reach the temporary blockage section during the blockage time or are affected by the

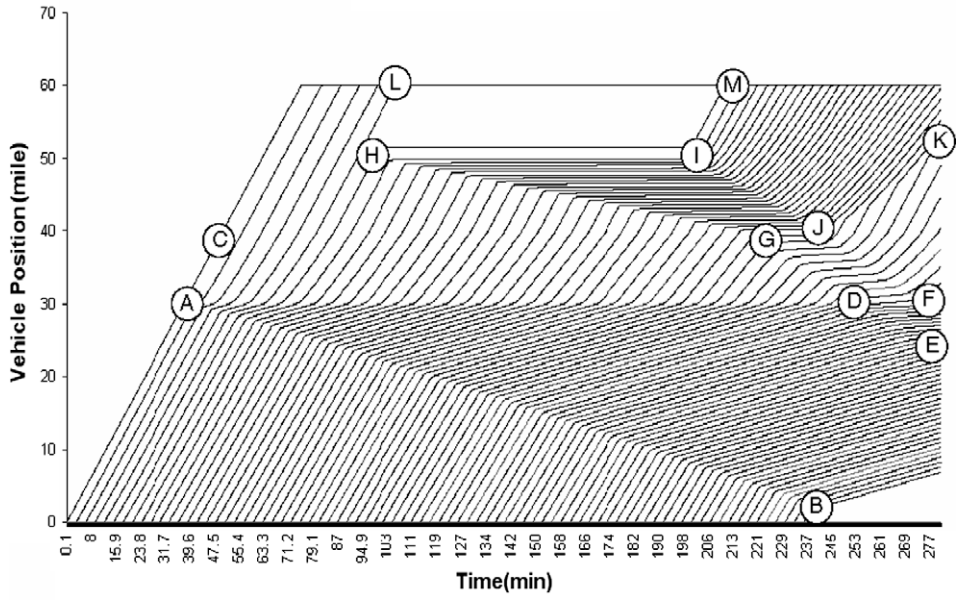

Fig. 6. AMS model test case space–time diagram (*SIR* length = 1000 ft).

blockage-induced backward-moving shockwave are entirely stopped until the discharge-induced backward-moving shockwave arrives. Upon discharging from the queue, vehicles start to discharge at a maximum flow rate.

The formation of various shockwaves resulting from varying traffic flow states caused by both the lane drop and the temporary roadway blockage is demonstrated in the space–time diagram. Wave *A–B* indicates the backward shockwave generated from vehicles entering the lane drop, while wave *A–D* indicates the stationary shockwave at the entrance of lane drop. Further, wave *C–G* is a stationary shockwave at the exit of the lane drop. Moreover, wave *H–G* corresponds to the backward shockwave caused by the temporary blockage. Wave *G–D* is the *H–G* shockwave propagated into the lane drop section, where the wave speed changes due to change of interfacing traffic states. The backward shockwave generated by discharge after the capacity of the temporary blockage is restored is represented by wave *I–J*. The same shockwave changes its speed upon entering the lane drop, wave *J–F*. Forward-moving shockwave *J–K* is also observed as the vehicles catches up to those slower vehicles (as they accelerate from a complete stop). Forward shockwaves captured by the AMS model includes *H–L*, *I–M*, and *J–K*. These wave speeds are not faster than the speeds of the actual flows that carry them, which is consistent with basic traffic flow properties.

Further examination of the shockwaves exhibited by the AMS model and those generated by the fundamental diagram Fig. 5b, demonstrates the AMS macroscopic properties. Shockwave *A–B* serves as an example. The speed of the backward shockwave *A–B* represented by the AMS model is found to be -0.14 ml/min = -8.4 mph, using Fig. 6. The shockwave *A–B* is caused by the traffic state transition from 3000 pcphpl (1500 pcphpl $\times$ two lanes) to 1782 pcphpl due to the lane drop. The corresponding densities and flows of the two traffic states are found to be 60.0 pc/ml and 227.6 pc/ml (Fig. 5b), resulting in a wave speed of $(3000 - 1782/(60.0 - 227.6)) = -0.12$ (ml/min) = -7.2 mph. The number captured by the AMS model is slightly higher than the theoretical figure. Note that this can be improved through proper calibration of model parameters.

5.2. Simulation of a freeway merging junction

The second simulation scenario highlights the traffic dynamic for AMS under the freeway merging situation. In the test network, two 3-lane freeways merge into one 5-lane freeway. Twenty miles downstream of the merging junction, a lane drop reduces the number of lanes from 5 to 3 (Fig. 7). The inbound freeway branch *B* has a constant inflow rate of 4000 vehicles per hour (vph), which is equivalent to 1333 vehicles/hour/lane (vphpl) between 0 and 120 min. The inbound branch *A* has a constant inflow rate of 7000 vph, which is equivalent to 2333 vphpl with a shorter time period between 30 and 60 min. The $\wp$ function and the simulation interval are kept the same as those used in the simulation scenario in Section 5.1.

The simulation follows the algorithmic steps described in Section 3. In particular, for vehicles whose *SIR* spans across the merging junction, the *SIR* is defined as illustrated as in the shaded area shown in Fig. 7. Moreover, Eq. (3) applies with x defined as the distance between the vehicle and the merging junction, and m and n are applied to as the number of lanes for the inbound branch and the outbound branch, respectively.

The space–time diagram of vehicles entering the network from inbound branches *A* and *B* are displayed in Fig. 8. Fig. 8(1) shows those from branch *A*, and Fig. 8(2) shows those from branch *B*. As shown in Fig. 8(2), vehicles traversing the merging junction prior to 30 min move at the free-flow speed. From 30 to 60 min, the *B* originated vehicles experience speed reduction at the merging junction (points (*a*)–(*b*) in Fig. 8(2)). It can be observed that these vehicles gradually recover their speed after passing the merging junction until they reach the downstream lane drop location (as shown as points (*d*) and (*f*) in Fig. 8). Fig. 8(2) also shows that a backward shockwave (*d*)–(*c*) is originated from the downstream lane drop because the inflow rate is greater than the capacity of the lane drop. Vehicles traversing the merging junction after 60 min join the slower moving vehicles, and the speed transition is depicted by the shockwave (*b*)–(*c*). When shockwaves (*d*)–(*c*) and (*b*)–(*c*) meet, the resultant wave (*c*)–(*e*) is formed between the free-flow moving vehicles and the lane drop induced traffic state. One can also see that similar space–time trajectories can be observed for vehicles originated from inbound branch *A*.

Additional numerical comparison was conducted to understand, at network and macroscopic levels, the comparison of AMS and the microscopic simulation model VISSIM using the same testing case. The same network and input flows were

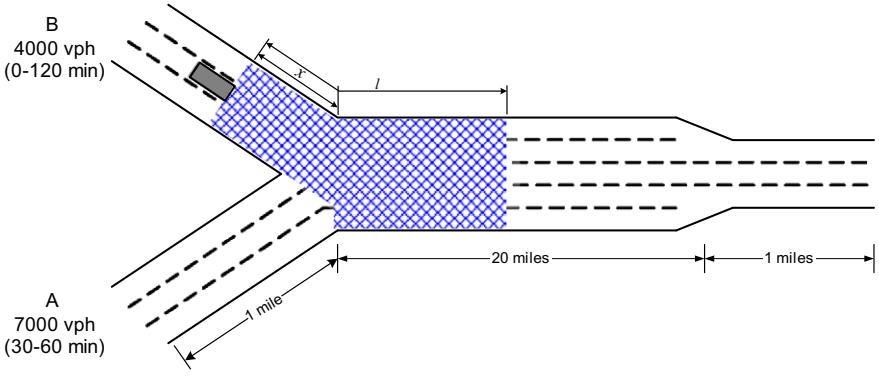

Fig. 7. Freeway merging scenario.

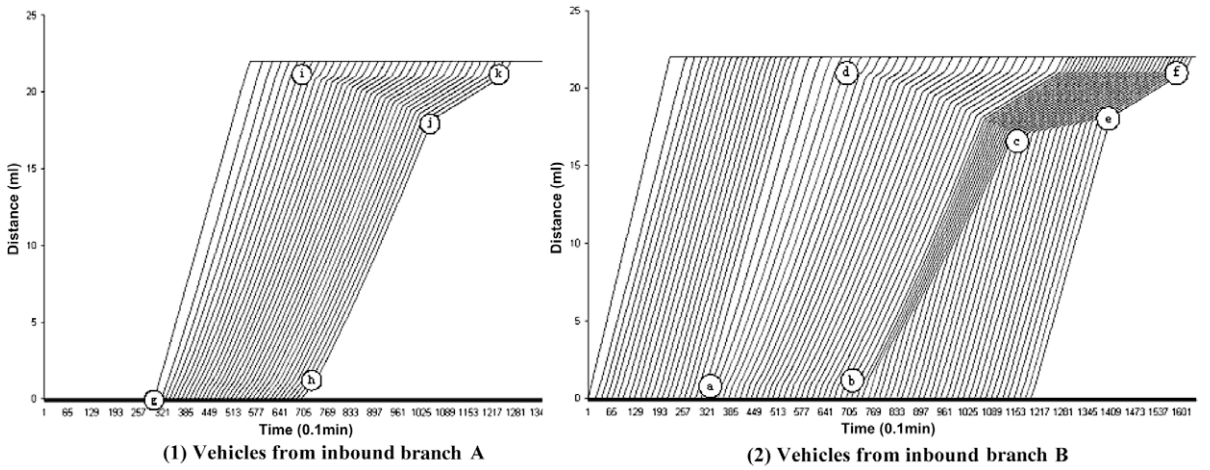

Fig. 8. Space–time diagram for the freeway merging case.

Table 1
Comparison of AMS and VISSIM in the freeway merging scenario.

Average travel time by VISSIM (min)	Average travel time by AMS (min)		Difference (%)
	(*SIR* length, ft)	(min)	
69.79	200	70.52	1.1
	220	69.91	0.1
	240	68.98	1.2
	260	68.55	1.8
	280	68.41	2.0
	300	67.94	2.7

specified in VISSIM to create the comparison case. As shown in Table 1, the average travel time from VISSIM is 69.79 min, whereas that for the AMS model varies according to the *SIR* length. The AMS travel time does not vary greatly due to changed *SIR* length. Furthermore, the difference is minimally (0.1%) with the *SIR* length set to be 220 ft. The differences for other *SIR* lengths range from 1.1% to 2.7%. Although this comparison may be short of theoretical rigor, it indicates, in a loosely quantitative manner, that AMS exhibits comparable macroscopic characteristics compared to a microscopic simulation model.

5.3. Flow distribution at a freeway merging junction

The further question of interest is how AMS depicts traffic under a variety of upstream inflow and downstream capacity conditions. In this simulation case, the simulation parameters are unchanged. The inflow of each upstream branch varies from 600 vph to 4800 vph (200 vphpl to 1600 vphpl). The v–k relation $\wp(k)$ is set as:

$$\wp(k) = \begin{cases} 63.87 & \forall\ k \le 23.0 \\ 63.87(1 - k/182.18)^{4.08} & \forall\ 23.0 \le k \le 182.18 \end{cases}$$

As such, the capacity of the downstream branch can be mathematically calculated to be 7100 vph.

Fig. 9 illustrates the simulated merging junction outflow for each inflow combination. The *X*-axis stands for the inflow for branch *A*, while the *Y*-axis is for branch *B*. Each dot stands for the simulated outflow according to each *A*, *B* flow combination. The dashed line stands for the downstream branch capacity at 7100 vph. For the outflow reading for each dot in the figure, simply draw a line in parallel to the dashed line and read the intercept of the line to either Y or X-axis. One can see that for all the inflow combinations, the simulated junction outflow equals the sum of both inflows if the sum is less than 7100 vph. On the other hand, the simulated junction outflow is capped at 7100 vph when the sum of the inflow is higher than 7100 vph. This means that the AMS simulation maintains a reasonable demand–supply relationship for a freeway merging junction.

Another issue of concern is the inbound branch flow distribution under various inflow combinations. As summarized in Table 2, q_A^i and q_B^i are the traffic inflows of branches *A* and *B*. q_A^o and q_B^o are the simulated outflows from upstream branches *A* and *B*. R_d is defined as the ratio of branch *A* inflow to branch *B* inflow; therefore, $R_d = q_A^i/q_B^i$. R_f is defined as the ratio of the branch *A* outflow to branch *B* outflow; thus, $R_f = q_A^o/q_B^o$. $(R_f - R_d)/R_d \cdot \%$ is defined as the percent deviation of outflow ratios to the inflow ratios. Given that both branches are freeway sections, no specific priority is given to any branch.

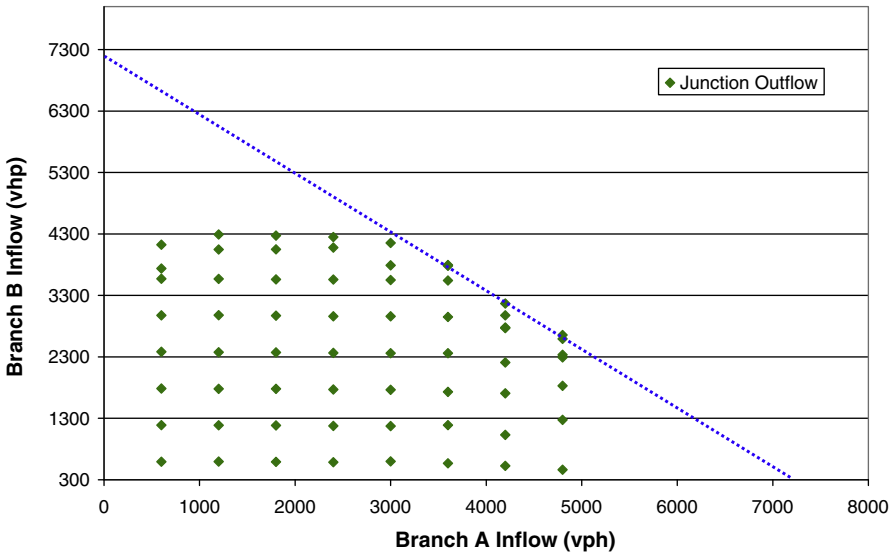

Fig. 9. AMS flow distribution for inbound branches *A* and *B*.

As can be seen From Table 2, $(R_f - R_d)/R_d \cdot \%$ in most cases are less than 2%, indicating that outflow distribution is similar to inflow distribution. This suggests that AMS simulations exhibit similar demand-based distribution characteristics as discussed by Jin (Jin, 2003).

6. Calibration of the AMS model

In addition to the encouraging analytical properties and numerical results, it is critical to demonstrate how to calibrate AMS model parameters with field data. The details of the model calibration are offered in this section.

6.1. Descriptions of field data

The AMS calibration task was carried out by using two I-80 dataset released by the Next-Generation Simulation (NGSIM) research program (NGSIM, 2005). The data presented in this research represent vehicle trajectories on the north-bound (east-bound) direction of Interstate 80 collected between 2:35 p.m. and 3:05 p.m. on December 3rd, 2003 (first prototype dataset) and during the afternoon peak period on April 13th, 2005 (I-80 dataset). There are three separate 15 min periods of data: (1) 4:00–4:15 p.m.; (2) 5:00–5:15 p.m.; and (3) 5:15–5:30 p.m. in the I-80 dataset. The first prototype dataset primarily represents free-flow traffic conditions. The first part of the I-80 dataset covers the period from 4:00 p.m. to 4:15 p.m., representing the onset of congestion. The remaining two periods represent peak-hour congested traffic conditions. The first prototype dataset contains trajectories for 4733 vehicles with nearly 3 million data points. The I-80 dataset for the 4:00–4:15 p.m. period, the 5:00–5:15 p.m. period and the 5:15–5:30 p.m. period contain 3366, 2589 and 3009 vehicle trajectories with about 1.25 million, 1.50 million and 1.75 million data points, respectively (NGSIM, 2005).

The NGSIM vehicle trajectory data files consist of millions of rows. Each row is a single *x*, *y*, *t* data point for a vehicle (specified by vehicle identification number) with associated information. There are 18 columns in each row. Five of these columns are used in the calibration process, including:

- Column 1: vehicle ID, i.e. vehicle identification number (ascending by time of entry into the study site).
- Column 2: frame ID, i.e. frame identification number (ascending by start time), unit: 1/15 of a second (first prototype dataset) and 1/10 of a second (I-80 dataset).
- Column 3: total frames, i.e. total number of frames in which the vehicle appears in this dataset.
- Column 6: local *Y*, i.e. longitudinal (*Y*) coordinate of the front center of the vehicle with respect to the entry edge of the section in the direction of travel.
- Column 14: lane identification, i.e. current lane position of vehicle. Lane 1 is the farthest left lane and lane 6 is the farthest right lane.

Table 2
Simulation results of AMS merge model.

q_A^i (vph)	q_B^i (vph)	q_{A1}^o (vph)	q_B^o (vph)	R_d	R_f	$\frac{(R_f-R_d)}{R_d}$ (%)
600	600	596	598	1.000	0.997	−0.3
	1200	599	1200	0.500	0.499	−0.2
	1800	600	1791	0.333	0.335	0.6
	2400	600	2384	0.250	0.252	0.8
	3000	599	2997	0.200	0.199	−0.5
	3600	597	3571	0.167	0.167	0
	4200	598	4128	0.143	0.145	1.4
	4800	595	4187	0.125	0.142	13.6
1200	600	1193	598	2.000	1.995	−0.3
	1200	1195	1192	1.000	1.003	0.3
	1800	1195	1788	0.667	0.668	0.2
	2400	1195	2380	0.500	0.502	0.4
	3000	1195	2981	0.400	0.401	0.35
	3600	1192	3597	0.333	0.331	−0.6
	4200	1192	4038	0.286	0.295	3.2
	4800	1194	4069	0.250	0.293	17.2
1800	600	1790	597	3.000	2.998	−0.1
	1200	1786	1193	1.500	1.497	−0.2
	1800	1791	1789	1.000	1.001	0.1
	2400	1787	2381	0.750	0.751	0.1
	3000	1788	2977	0.600	0.601	0.2
	3600	1789	3540	0.500	0.505	1.0
	4200	1788	4120	0.429	0.434	1.2
	4800	1789	4287	0.375	0.417	11.2
2400	600	2388	594	4.000	4.020	0.5
	1200	2382	1192	2.000	1.998	−0.1
	1800	2384	1787	1.333	1.334	0.1
	2400	2384	2382	1.000	1.001	0.1
	3000	2388	2982	0.800	0.801	0.1
	3600	2388	3571	0.667	0.669	0.3
	4200	2382	4027	0.571	0.592	3.7
	4800	2374	4256	0.500	0.558	11.6
3000	600	2983	595	5.000	5.013	0.3
	1200	2983	1195	2.500	2.496	−0.2
	1800	2980	1789	1.667	1.666	−0.1
	2400	2978	2382	1.250	1.250	0
	3000	2982	2978	1.000	1.001	0.1
	3600	2979	3572	0.833	0.834	0.1
	4200	2981	3998	0.714	0.746	4.5
	4800	2982	4150	0.625	0.719	15.0
3600	600	3575	597	6.000	5.988	−0.2
	1200	3573	1195	3.000	2.990	−0.3
	1800	3571	1791	2.000	1.994	−0.3
	2400	3572	2387	1.500	1.496	−0.3
	3000	3568	2983	1.200	1.196	−0.3
	3600	3570	3573	1.000	0.999	−0.1
	4200	3432	3937	0.857	0.872	1.8
	4800	3275	4181	0.750	0.783	4.4
4200	600	4125	599	7.000	6.886	−1.6
	1200	4055	1191	3.500	3.405	−2.7
	1800	4079	1770	2.333	2.305	−1.2
	2400	4092	2386	1.750	1.715	−2.0
	3000	3789	3000	1.400	1.263	−9.8
	3600	3818	3564	1.167	1.071	−8.2
	4200	3389	3788	1.000	0.895	−10.5
	4800	3170	3921	0.875	0.809	−7.5
4800	600	3740	598	8.000	6.254	−21.8
	1200	4299	1193	4.000	3.604	−9.9
	1800	4286	1788	2.667	2.397	−10.1
	2400	4271	2379	2.000	1.795	−10.3
	3000	4235	2920	1.600	1.450	−9.4
	3600	4024	3372	1.333	1.193	−10.5
	4200	3737	3230	1.143	1.157	1.2
	4800	3394	3999	1.000	0.849	−15.1

6.2. Model calibration approach and procedure

Before discussing the calibration procedure, the two modified two-regime Greenshield's models used in this effort are introduced. The first model, as shown in Eq. (14), is employed by the supply simulator model of DynaMIT – hereafter referred to as the G1 model (Ben-Akiva et al., 1998); the second model, as shown in Eq. (15), is used in DYNASMART – hereafter referred to as the G2 model (Jayakrishnan et al., 1994). The objective of calibration is to determine the optimal values for the *SIR* length and its corresponding parameters (v_f, k_{jam}, k_b, α, and β (for G1 model only)) that best fit the NGSIM data.

$$v^{cal} = \begin{cases} v_f, & k \le k_b \\ v_f\left[1 - \left(\frac{k-k_b}{k_{jam}-k_b}\right)^{\beta}\right]^{\alpha}, & k_b \le k \le k_{jam} \end{cases} \tag{14}$$

$$v^{cal} = \begin{cases} v_f, & k \le k_b \\ v_f\left[1 - \left(\frac{k-k_b}{k_{jam}-k_b}\right)\right]^{\alpha}, & k_b \le k \le k_{jam} \end{cases} \tag{15}$$

where, v^{cal} is the speed calculated according to the two-regime equation with AMS (mph), k the density in a certain Speed Influencing Region (veh/ml/ln), k_b the maximum density that sustains free-flow speed, parameter to be calibrated, k_{jam} the jam density, parameter to be calibrated, v_f the free-flow speed, parameter to be calibrated, α the parameter to be calibrated, and β is the parameter to be calibrated (G1 model only).

Recall that the AMS simulation mechanism relies on the *SIR* density function $\wp(\cdot)$ and the parameters to be calibrated, which are the *SIR* length and the parameters in $\wp(\cdot)$. As depicted in Fig. 10 in the overall calibration procedure *SIR* length l was set between 100 and 500 ft with a 25-ft increment. For a given *SIR* length l, the average speed and *SIR* density were processed and calculated from the NGSIM raw data for each vehicle and every simulation interval. For each *SIR* length l, the calculation creates more than 160,000 data points $(k_i^{t-\Delta t,obs}, v_i^{t,obs})$ from the NGSIM dataset.

The same observed *SIR* density data $k_i^{t-\Delta t,\ obs}$ were applied into the assumed speed–density function to obtain the calculated speed $v_i^{t,\ cal}$. Both calculated and observed speed variables constituted the residual column matrix

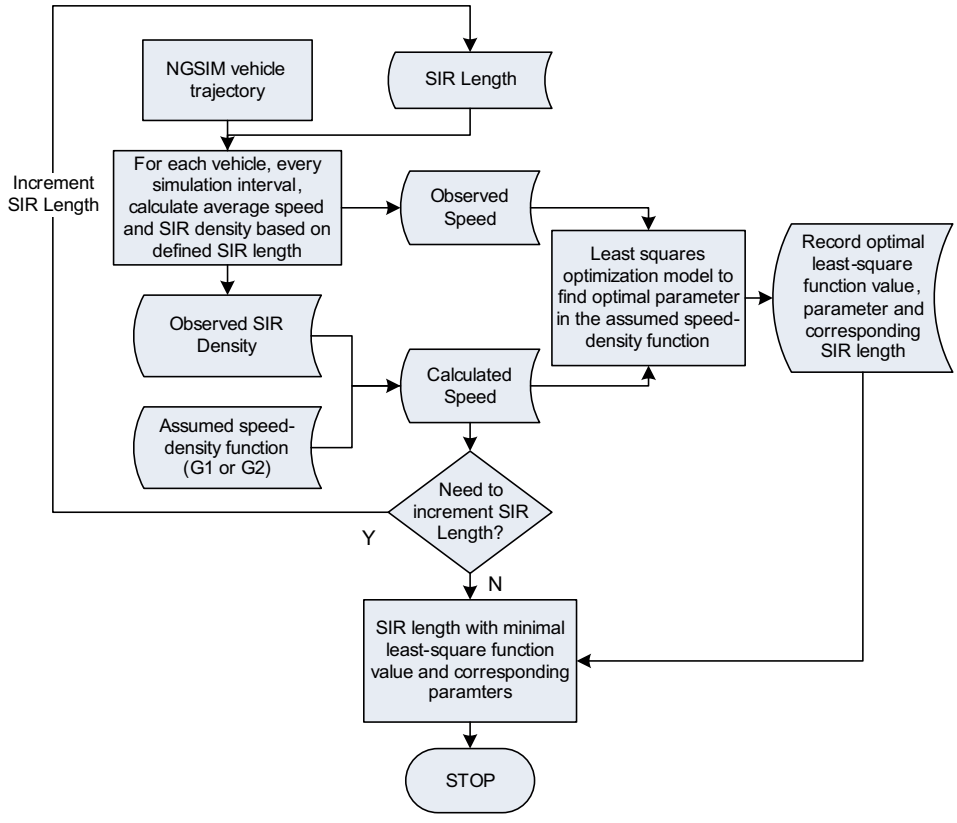

Fig. 10. Calibration procedure.

$X = [(v_1^{cal} - v_1^{obs}), \ldots, (v_i^{cal} - v_i^{obs}), \ldots]^T$, where i is the subscript denoting the ith data point and v_i^{obs} is the ith observed speed in NGSIM dataset. The resulting least-square problem can be expressed as

$$\min_{v_f,\alpha,\beta,k_b,k_{jam}} f = \frac{1}{2}X^T X \quad \text{subject to } v_f > 0; \alpha > 0; \beta > 0; 0 < k_b < k_{jam} \tag{16}$$

The objective was to minimize the sum of the square of the deviations between the observed and calculated speeds for all data points by solving for the optimal model parameters such as v_f, α, β, k_b, and k_{jam}. Many well-established algorithms, such as Newton's Method, Gauss–Newton's Method and Levenberg–Marquadt Method, exist to solve this problem. The MATLAB function *lsqcurvefit* was used in this calibration effort. After solving the least-squares problem, the optimal parameters and corresponding *SIR* length were recorded. The *SIR* length was further incremented based on a predefined increment (e.g. 25 ft) and the entire process was repeated until all the candidate *SIR* lengths were examined. The complete process was repeated separately for both the G1 and G2 models.

6.3. Calibration results

Table 3 lists all the optimal parameters associated with each *SIR* length for both the G1 and G2 models. Judging from the least-square function values shown in Table 3, for the G1 model, the optimal *SIR* length is found to be 225 ft, and the optimal parameter values are: free-flow speed v_f = 61.23 mph; jam density k_{jam} = 185.27 veh/ml/ln; and the two-regime cut-off density = 31.36 veh/ml/ln. In addition, the value for α and β is 1.94 and 0.50, respectively. The optimal *SIR* length for the G2 model appears to be the same, 225 ft. The optimal parameter values are: free-flow speed v_f = 63.87 mph; jam density k_{jam} = 182.18 veh/ml/ln; and two-regime cut-off density = 22.85 veh/ml/ln. Moreover, the optimal α value is 4.08. These results show that the calibrated parameter values for both models are comparable.

Examining the least-squares function values for different *SIR* lengths for both G1 and G2 models as shown in Fig. 11, one can find two convex curves, the nadir of the curve stands for the *SIR* length permitting the best fit. The optimal *SIR* length

Table 3
Calibration results of Greenshield's models 1 and 2.

SIR length (ft)	v_f (mph)	k_{jam} (veh/ml/ln)	k_b (veh/ml/ln)	α	β	F (ml∗ml/h/h)
G1 model						
100	60.161	186.435	30.004	1.61	0.42	2476688.90
125	59.046	185.307	27.581	1.88	0.53	2112413.47
150	64.124	193.94	22.265	2.55	0.68	1971397.55
175	60.405	185.171	29.614	1.99	0.54	1867050.37
200	62.58	185.346	31.254	1.91	0.49	1852751.07
225	**61.233**	**185.266**	**31.361**	**1.94**	**0.50**	**1794331.19**
250	62.897	185.272	30.715	2.00	0.51	1809755.73
275	62.062	185.285	31.677	1.93	0.49	1824607.10
300	63.589	185.293	30.648	2.01	0.51	1886354.76
325	64.611	185.305	30.849	1.96	0.48	1990042.20
350	63.588	185.308	30.289	2.02	0.51	2031743.43
375	63.23	185.371	30.93	1.92	0.48	2119347.00
400	63.523	185.486	31.187	1.84	0.45	2242453.54
425	63.682	185.407	30.438	1.86	0.46	2353016.02
450	64.451	185.417	29.993	1.84	0.45	2503827.90
475	64.818	190.063	25.973	2.32	0.59	2613741.17
500	63.93	190.125	24.221	2.51	0.65	2709079.86
G2 model						
100	60.737	212.943	12.835	4.01	–	2326386.11
125	62.392	186.637	13.970	3.48	–	2122940.33
150	62.594	186.139	18.487	3.77	–	1987370.10
175	62.299	185.307	21.798	3.98	–	1914209.79
200	62.601	184.929	23.703	4.17	–	1878530.95
225	**63.868**	**182.184**	**22.852**	**4.08**	–	**1850805.45**
250	63.669	182.136	24.827	4.29	–	1873055.97
275	63.982	182.243	25.138	4.36	–	1915219.47
300	64.332	182.29	25.775	4.50	–	1983079.77
325	64.45	182.326	26.198	4.59	–	2072796.61
350	64.755	182.498	26.516	4.72	–	2175600.74
375	64.579	182.456	27.248	4.86	–	2303820.51
400	64.699	188.825	27.477	5.19	–	2442971.36
425	64.851	182.625	27.589	5.06	–	2598406.94
450	64.927	186.838	27.819	5.33	–	2761852.87
475	64.903	189.735	28.091	5.56	–	2944527.88
500	64.151	187.037	27.871	5.52	–	3121991.82

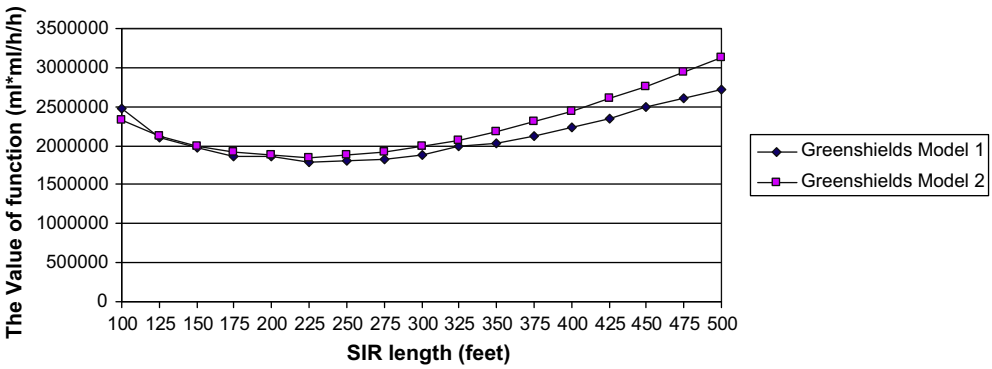

Fig. 11. Illustration of calibration results.

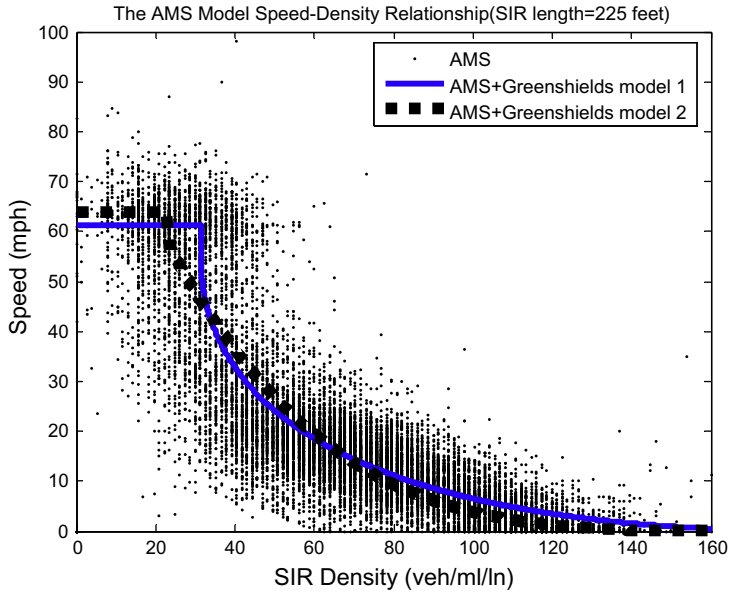

Fig. 12. AMS model speed–density relationship (*SIR* length = 225 ft).

appears to be 225 ft. This number suggests that during light traffic conditions, such as level of service *A* (k = 11 veh/ml/ln, average spacing = 480 ft) or *B* (k = 18 veh/ml/ln, average spacing = 293 ft), vehicles are likely to be at free-flow speed, or responding to only one leading vehicle most of the time. When traffic gets more congested, such as level of service *C* (k = 26 veh/ml/ln, average spacing = 203 ft), *D* (k = 35 veh/ml/ln, average spacing = 150 ft), and *E* (k = 45 veh/ml/ln, average spacing = 117 ft), a vehicle's speed is more likely to be frequently affected by more than one leading vehicles. This is analogous to the concept of the anticipative car-following theory (Lenz et al., 1999).

For Greenshield's model of interest, the curves based on the 225-ft *SIR* length and associated optimal parameter values are plotted in Fig. 12, along with all the speed-*SIR* density data points. One should note that this is not a typical v–k diagram because the x-axis is the *SIR* density based on the 225 *SIR* length and each point is obtained by taking the average over the simulation interval (6 s) over all the collected data for all vehicles in this case. It appears that both curves fit the data fairly well, and the jam density and two-regime cut-off density point are in the range consistent with that established in the literature, although the density definition in this paper is different from a typical density definition.

7. Discussion and concluding remarks

This paper presents an Anisotropic Mesoscopic Simulation (AMS) model that explicitly captures the anisotropic properties of traffic flows. The Anisotropic Mesoscopic Simulation (AMS) model is a vehicle-based model that explicitly incorporates the concept of the car-following mechanism. The anisotropic traffic flow properties can be intuitively observed as

vehicles' speeds are mainly influenced by average traffic conditions in front of the vehicles. Through both analytical and numerical analysis, this proposed model was shown to exhibit satisfactory traffic flow properties.

The discussions focus on the key modeling concepts, analytical properties and numerical analysis, and the calibration process and results. The addressed analytical properties are the overtaking conditions, acceleration and deceleration rate bounds, and shockwaves. The numerical analysis includes both freeway segments as well as merging junctions. Considerable efforts were devoted to employ the Next-Generation Simulation (NGSIM) program datasets to calibrate the AMS model parameters. The NGSIM data are the unique data source that was used to extract all the information needed for AMS model calibration. The results satisfactorily validate the AMS model, and the *SIR* length and its corresponding parameter values best fit the datasets have been found.

In addition to the improved anisotropic traffic dynamic properties compared with traditional queue-server type mesoscopic models, the computational advantage of AMS can be also intuitively observed from the memory storage and temporal scalability when compared with other anisotropic cell-based type of models such as CTM. AMS operates on a node-arc network representation, which is generally more memory efficient and temporally scalable than cell-based models from the standpoint of storing network-related attributes. For a cell-based simulation approach, if for any reason that the simulation interval needs to be changed, the entire cell network structure needs to be rebuilt; on the other hand, changing simulation interval would not affect network structure representation in AMS. As shown in Section 3, in AMS, required computation time is generally linear to number of vehicles present in the network. This ensures desirable computational tractability.

This presented study is part of a wider effort that focuses on the development of generalized mesoscopic modeling capability for DTA applications. The ongoing research activities include network merging junctions with priorities (e.g. freeway main-lanes versus on-ramps), weaving sections, heterogeneous *SIR* length based on facilities or traffic conditions, and the determination of the optimal simulation interval through calibration. Moreover, the development of AMS on interrupted flow facilities such as signalized intersection is also underway.

Acknowledgements

This research is supported by the National Science Foundation (NSF) Project SCI-0332001 (2003–2006). The authors thank FHWA NGSIM program for making the vehicle trajectory datasets available for the calibration task. The anonymous reviewers made constructive comments that have led to significant improvement of this paper, and their review and assistance are acknowledged. All the opinions, findings and conclusions expressed in this research are from the authors and do not necessarily reflect the viewpoints of the funding agency.

Appendix A. – Notations

i	subscript for vehicles
d_i	distance between vehicle i and trailing vehicle $i-1$
n	total number of vehicles present within vehicle i's *SIR*, excluding vehicle i
S_i	Speed Influencing Region for vehicle i
l	length of S_i, assumed to be the same for all vehicles
h_i^{i+n}	distance from vehicle $i+n$ to the front boundary of S_i, measured from the center of a vehicle, $h_i^i = l$.
Δ	duration of a simulation interval
v_f	free-flow speed, assumed to be the same for all vehicles
v_i	speed of vehicle i
k_i	*SIR* density of vehicle i, $k_i = n/l$
t	beginning time instant of the simulation time interval $[t, t+\Delta]$
$\wp : k \to v$	non-increasing function specifying the speed–density relationship of vehicle progression, $\wp(0) = v_f$ and $\wp(k_{jam}) = 0$
k_{jam}	jam density
c_{jam}	minimum spacing between vehicles, $c_{jam} = 1/k_{jam}$
n_{jam}	maximum number of vehicles within a Speed Influencing Region
y_i^t	distance of vehicle i to downstream stop bar at time t

As shown in Fig. 13, a vehicle stream is present in a single lane highway. Vehicle i has n leading vehicles ($i+1$ to $i+n$) within its *SIR*. The *SIR* length is assumed to be l for all vehicles of interest. The distance between each of these n vehicles (vehicle k) and the front end of *SIR* for vehicle i is assumed to be h_i^{i+k}, where $i+k$ is the identification number of the kth vehicle in front of vehicle i. Vehicle $i-1$ approaches vehicle i at a higher or equal speed by definition. At the beginning of the simulation interval Δ, the distance between vehicles i and $i-1$ is d_i.

At the beginning of a simulation interval $[t, t+\Delta]$, the prevailing speeds of vehicle $i-1$ and i, $v_{i-1}(t)$ and $v_i(t)$, can be evaluated by $\wp : k \to v$ given their respective *SIR* densities. The *SIR* density k_i equals n/l, whereas, the *SIR* density k_{i-1} is determined based on d_i, which is the distance between vehicle $i-1$ and i, and the locations of vehicles in S_i, represented by $h_i^1, h_i^2, \ldots, h_i^{i+n}$.

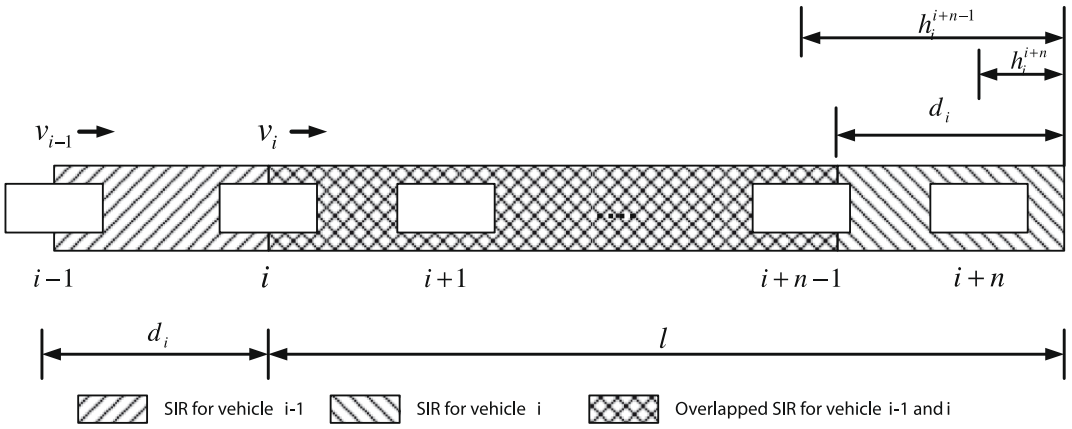

Fig. 13. Schematic for the proof of overtaking condition.

Appendix B

Proof for Lemma 1

Overtaking requires that vehicle $i-1$ travels at a higher speed than its leading vehicle i. Since vehicle i has n leading vehicles in its *SIR*, vehicle $i-1$ needs to have a fewer number of leading vehicles to exhibit a higher speed. According to Fig. 13, if there are at least two vehicles existing between the vehicle $i-1$ and i's *SIR* front end, then vehicle $i-1$ has less number of vehicles present in its *SIR* compared with vehicle i. Q.E.D.

Appendix C

Proof for Theorem 1 (Non-overtaking sufficient condition)

Given the speed–density function shown in Fig. 14 and the condition that vehicle $i-1$ travels at a higher speed than vehicle i, without loss of generality, d_i always satisfies one and only one condition listed in Table 4 at the beginning of the simulation interval Δ. Based on the respective *SIR* density, the shortened distance between vehicles i and $i-1$ for each d_i condition by simulation is listed on the right-side column. Deriving the non-overtaking condition is equivalent to showing that regardless of what condition d_i falls into at the beginning of any simulation interval, the distance between vehicle $i-1$ and i at the end of that particular simulation interval is not greater than d_i.

As depicted in Table 4, in a general case in which $h_i^{i+n-m} < d_i \leqslant h_i^{i+n-m-1}, \forall\ m = 0, \ldots, n$, the distance shortened is $[\wp((n-m)/l) - \wp(n/l)]\Delta$. It is also true that $m \cdot c_{jam} \leq h_i^{i+n-m}$ because h_i^{i+n-m} is the distance of the $(n-m)$th vehicle to the front end of S_i, and h_i^{i+n-m} must be no shorter than that occupied by m vehicles at jam density, i.e. m/k_{jam} space. The sufficient condition is to guarantee that for all possible d_i conditions, inequality (17) always holds. That is,

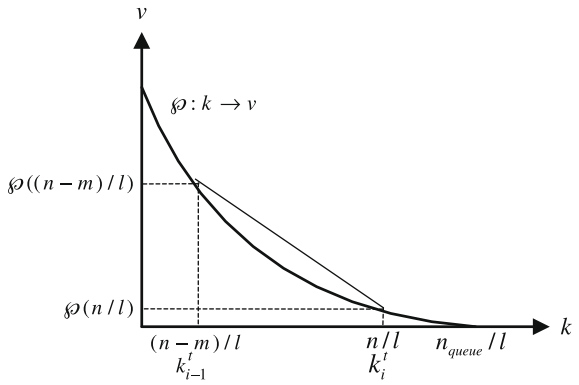

Fig. 14. Speed–density function used in the AMS simulation.

Table 4
Possible conditions of d_i and respective shortened distance between vehicle i and $i-1$ during simulation Δ.

Possible conditions for d_i ($d_i > 0$)	k_{i-1}	k_i	Distance shortened between vehicle $i-1$ and i at the end of simulation interval $(t+\Delta)$
$h_i^i < d_i$	$0/l$	n/l	$[\wp(0) - \wp(n/l)]\Delta$
$h_i^{i+1} < d_i \le h_i^i$	$1/l$	n/l	$[\wp(1/l) - \wp(n/l)]\Delta$
$\vdots$	$\vdots$	n/l	$\vdots$
$h_i^{i+n-m} < d_i \le h_i^{i+n-m-1}$	$n-m/l$	n/l	$[\wp(n-m/l) - \wp(n/l)]\Delta$
$\vdots$	$\vdots$	n/l	$\vdots$
$h_i^{i+n-2} < d_i \le h_i^{i+n-3}$	$n-2/l$	n/l	$[\wp(n-2/l) - \wp(n/l)]\Delta$
$h_i^{i+n-1} < d_i \le h_i^{i+n-2}$	$n-1/l$	n/l	$[\wp(n-1/l) - \wp(n/l)]\Delta$
$h_i^{i+n} < d_i \le h_i^{i+n-1}$	n/l	n/l	0

$$d_i > [\wp((n-m)/l) - \wp(n/l)]\Delta, \quad \forall\ 0 \le m \le n, 0 \le n \le n_{jam} \tag{17}$$

Because $d_i > h_i^{i+n-m} \ge m/k_{jam}$, therefore, $m/k_{jam} > [\wp((n-m)/l) - \wp(n/l)]\Delta$ implies $d_i > [\wp((n-m)/l) - \wp(n/l)]\Delta$.

Furthermore, we have:

$$\frac{m}{k_{jam}} > [\wp((n-m)/l) - \wp(n/l)]\Delta \Rightarrow \frac{l}{\Delta \cdot k_{jam}} > \frac{\left[\wp(k_{i-1}^t) - \wp(k_i^t)\right]}{k_i^t - k_{i-1}^t} \Rightarrow \frac{l}{\Delta \cdot k_{jam}} > \frac{\left[\wp(k_{i-1}^t) - \wp(k_i^t)\right]}{k_i^t - k_{i-1}^t} \Rightarrow$$
$$-\frac{l}{\Delta \cdot k_{jam}} < -\frac{\left[\wp(k_{i-1}^t) - \wp(k_i^t)\right]}{k_i^t - k_{i-1}^t}, \quad \forall\ 0 \le m \le n, 0 \le n \le n_{jam} \tag{18}$$

Obviously, $-\frac{[\wp(k_{i-1}^t) - \wp(k_i^t)]}{k_i^t - k_{i-1}^t}$ is the slope of the line connecting $\left[k_{i-1}^t, \wp(k_{i-1}^t)\right]$ and $\left[k_i^t, \wp(k_i^t)\right]$. Establishing the sufficient condition is equivalent to finding $\inf\left\{-\frac{[\wp(k_{i-1}^t) - \wp(k_i^t)]}{k_i^t - k_{i-1}^t}\right\}$. Without loss of generality, if $\wp$ is differentiable everywhere, $\inf\left\{-\frac{[\wp(k_{i-1}^t) - \wp(k_i^t)]}{k_i^t - k_{i-1}^t}\right\}$ can be represented as $\min_k(\wp')$. The sufficient condition for non-overtaking hence becomes $-\frac{l}{\Delta \cdot k_{jam}} < \min(\wp') \Rightarrow l > -\min(\wp') \cdot \Delta \cdot k_{jam}$.

Appendix D

Proof for Theorem 2 (Overtaking sufficient condition)

Given the speed–density function shown in Fig. 14 and following the inequality $d_i \le h_i^{i+n-m-1},\ \forall\ m = 0, \ldots, n$ in Table 4, the shortened distance is $[\wp(n-m/l) - \wp(n/l)]\Delta$. If $d_i < [\wp(n-m/l) - \wp(n/l)]\Delta$, then overtaking occurs. It is also true that $h_i^{i+n-m-1} \leqslant l - \frac{n-m}{k_{jam}}$; therefore, if $l - \frac{n-m}{k_{jam}} < [\wp(n-m/l) - \wp(n/l)]\Delta$ then $d_i < [\wp(n-m/l) - \wp(n/l)]\Delta$.

$l - \frac{n-m}{k_{jam}} < [\wp(n-m/l) - \wp(n/l)]\Delta$ can be re-written as:

$$\frac{[\wp(n-m/l) - \wp(n/l)]}{m/l} > \frac{l}{m}\left(l - \frac{n-m}{\Delta \cdot k_{jam}}\right) \Rightarrow \frac{\wp(k_{i-1}^t) - \wp(k_i^t)}{k_i^t - k_{i-1}^t} > \frac{(l \cdot k_{jam} - l \cdot k_{i-1}^t) \cdot l}{\Delta(k_i^t - k_{i-1}^t) \cdot l \cdot k_{jam}}$$
$$\Rightarrow \frac{\wp(k_{i-1}^t) - \wp(k_i^t)}{k_i^t - k_{i-1}^t} > \frac{l}{\Delta \cdot k_{jam}} \cdot \frac{(k_{jam} - k_{i-1}^t)}{(k_i^t - k_{i-1}^t)} \Rightarrow -\frac{\wp(k_{i-1}^t) - \wp(k_i^t)}{k_i^t - k_{i-1}^t} < -\frac{l}{\Delta \cdot k_{jam}} \cdot \frac{(k_{jam} - k_{i-1}^t)}{(k_i^t - k_{i-1}^t)}$$
$$\Rightarrow l < \Delta \cdot k_{jam} \cdot \frac{\wp(k_{i-1}^t) - \wp(k_i^t)}{(k_{jam} - k_{i-1}^t)} \qquad \text{Q.E.D.}$$

Appendix E

Proof for deceleration and acceleration bounds

Given that vehicle $i-1$ is decelerating, the deceleration/acceleration of vehicle $i-1$ at time t can be expressed as

$$a_{i-1}^t = \frac{\wp(k_{i-1}^t) - \wp(k_{i-1}^{t-1})}{\Delta} \tag{19}$$

The change in distance between vehicle $i-1$ and i during Δ is $[\wp(k_{i-1}^{t-1}) - \wp(k_i^{t-1})]\Delta$. The maximal number of vehicles that can be accommodated into such distance is $[\wp(k_{i-1}^{t-1}) - \wp(k_i^{t-1})]\Delta \cdot k_{jam}$. As a result, the change of *SIR* density for vehicle $i-1$ at time t Δk_{i-1}^t is bounded by inequality:

$$\Delta k_{i-1}^{t} \leq \frac{\left[\wp(k_{i-1}^{t-1}) - \wp(k_{i}^{t-1})\right]\Delta \cdot k_{jam}}{l} \tag{20}$$

Let $\lambda = \frac{\left[\wp(k_{i-1}^{t-1}) - \wp(k_{i}^{t-1})\right]\cdot k_{jam}}{l}$, Eq. (20) can be expressed as $\Delta k_{i-1}^{t} \leq \lambda \cdot \Delta$.

From Eq. (19), we have

$$a_{i-1}^{t} = \frac{\wp(k_{i-1}^{t}) - \wp(k_{i-1}^{t-1})}{\Delta} = \frac{\wp(k_{i-1}^{t-1} + \Delta k_{i-1}^{t-1}) - \wp(k_{i-1}^{t-1})}{\Delta}$$

For deceleration, $\lambda > 0$, therefore $0 \geq \frac{\wp(k_{i-1}^{t-1}+\Delta k_{i-1}^{t-1}) - \wp(k_{i-1}^{t-1})}{\Delta} \geq \frac{\wp(k_{i-1}^{t-1}+\lambda\Delta) - \wp(k_{i-1}^{t-1})}{\Delta}$

For acceleration, $\lambda < 0$, therefore $0 \leq \frac{\wp(k_{i-1}^{t-1}+\Delta k_{i-1}^{t-1}) - \wp(k_{i-1}^{t-1})}{\Delta} \leq \frac{\wp(k_{i-1}^{t-1}+\lambda\Delta) - \wp(k_{i-1}^{t-1})}{\Delta}$

$\wp(k_{i-1}^{t-1} + \lambda\Delta)$ can be expressed as a Taylor Series, that is:

$$\wp(k_{i-1}^{t-1} + \lambda\Delta) = \wp(k_{i-1}^{t-1}) + \wp'(k_{i-1}^{t-1})(\lambda\Delta) + \frac{\wp''(k_{i-1}^{t-1})}{2!}(\lambda\Delta)^2 + \frac{\wp'''(k_{i-1}^{t-1})}{3!}(\lambda\Delta)^3 + \cdots$$

Therefore, the deceleration bounds for vehicle $i-1$ at time t can be expressed as:

$$0 \geq a_{i-1}^{t} \geq \wp'(k_{i-1}^{t-1})\lambda + \frac{\wp''(k_{i-1}^{t-1})}{2!}\lambda^2\Delta + \frac{\wp'''(k_{i-1}^{t-1})}{3!}\lambda^3\Delta^2 + \cdots,$$
$$\lambda = \frac{\left[\wp(k_{i-1}^{t-1}) - \wp(k_{i}^{t-1})\right]\cdot k_{jam}}{l} > 0$$

Similarly, the acceleration bounds for vehicle $i-1$ at time t can be expressed as:

$$0 \leq a_{i-1}^{t} \leq \wp'(k_{i-1}^{t-1})\lambda + \frac{\wp''(k_{i-1}^{t-1})}{2!}\lambda^2\Delta + \frac{\wp'''(k_{i-1}^{t-1})}{3!}\lambda^3\Delta^2 + \cdots,$$
$$\lambda = \frac{\left[\wp(k_{i-1}^{t-1}) - \wp(k_{i}^{t-1})\right]\cdot k_{jam}}{l} < 0 \quad \text{Q.E.D.}$$

Appendix F

Proof for AMS Shockwave Speed

As illustrated in Fig. 15, assuming that vehicles $i+1, i+2, \ldots$ are in a standing-still queue, with the corresponding spacing $\frac{l}{m}$. Vehicles $i, i-1, i-2, \ldots$ are assumed to averagely have spacing $\frac{l}{n}$ and $n < m$. Vehicles $i, i-1, i-2, \ldots$ have non-zero speed because $\frac{l}{n} > \frac{l}{m}$.

The backward shockwave speed between two states ω can be calculated using a typical flow–density fundamental diagram approach as Eq. (21):

$$\omega_{12} = \frac{q_1 - q_2}{k_1 - k_2} \tag{21}$$

Subsequently, the shockwave can be calculated as:

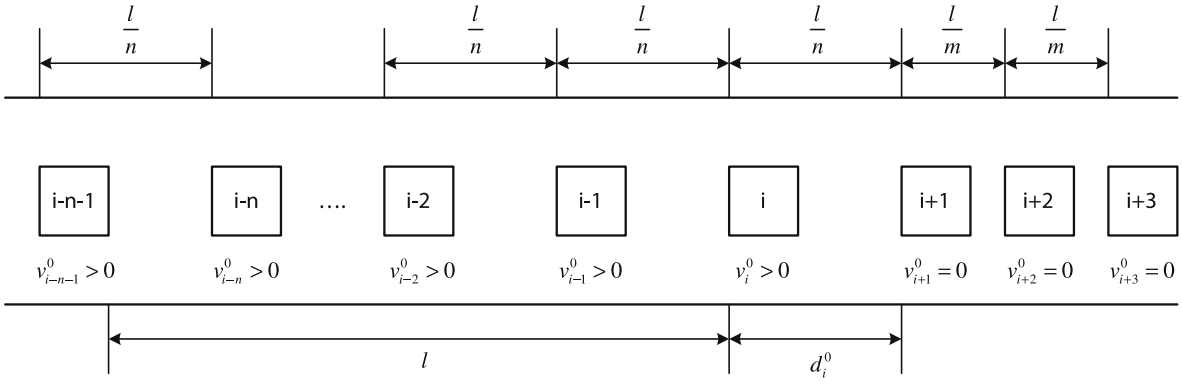

Fig. 15. Schematic for the derivation of shockwave speed.

$$q_2 = kv = \frac{n}{l}\cdot v_f\left(1-\frac{n/l}{m/l}\right) = \frac{n}{l}\cdot v_f\cdot\frac{m-n}{m}$$
$$\omega_1 = \frac{\Delta q}{\Delta k} = \frac{q_1-q_2}{k_1-k_2} = \frac{0-v_f\cdot\frac{n}{l}\cdot\frac{m-n}{m}}{\frac{m}{l}-\frac{n}{l}} = -\frac{n}{m}\cdot v_f$$

The shockwave depicted by the AMS can be shown by determining how many vehicles join the tail of the standing-still queue after one simulation time interval Δ. Denoting the distance between vehicle i and the immediate leading vehicle $i+1$ at time $t=0$ as $d_i^0 = \frac{l}{n}$, the corresponding vehicle i speed can be calculated as:

$$d_i^0 = \frac{l}{n} \Rightarrow k_i^0 = \frac{1+\frac{m}{l}\left(l-\frac{l}{n}\right)}{l} = \frac{1}{l}+\frac{m}{l}\left(1-\frac{1}{n}\right) \Rightarrow v_i^0 = v_f\left(1-\frac{1}{m}-1+\frac{1}{n}\right) = v_f\cdot\left(\frac{1}{n}-\frac{1}{m}\right)$$

After one simulation interval Δ, the spacing between vehicles i and $i+1$ is reduced to $d_i^\Delta = \frac{l}{n} - v_f\cdot\Delta\cdot\left(\frac{1}{n}-\frac{1}{m}\right) = \frac{l}{m}$. This means that the speed of vehicle i becomes zero after the position update.

Similarly, the spacing between vehicles $i-1$ and i is also reduced to $\frac{l}{m}$ as shown below.

$$d_{i-1}^0 = \frac{l}{n} \Rightarrow k_{i-1}^0 = \frac{2+\frac{m}{l}\left(l-\frac{2l}{n}\right)}{l} = \frac{2}{l}+\frac{m}{l}\left(1-\frac{2}{n}\right) \Rightarrow v_{i-1}^0 = v_f\left(1-\frac{2}{m}-1+\frac{2}{n}\right) = v_f\left(\frac{2}{n}-\frac{2}{m}\right) \Rightarrow d_{i-1}^\Delta = \frac{l}{n} - (v_{i-1}^0 - v_i^0)$$
$$= \frac{l}{n} - v_f\left(\frac{2}{n}-\frac{2}{m}-\frac{1}{n}+\frac{1}{m}\right)\cdot\Delta = \frac{l}{n} - v_f\cdot\left(\frac{1}{n}-\frac{1}{m}\right)\cdot\Delta = \frac{l}{m}.$$

$$d_{i-2}^0 = \frac{l}{n} \Rightarrow k_{i-2}^0 = \frac{3+\frac{m}{l}\left(l-\frac{3l}{n}\right)}{l} = \frac{3}{l}+\frac{m}{l}\left(1-\frac{3}{n}\right) \Rightarrow v_{i-2}^0 = v_f\left(1-\frac{3}{m}-1+\frac{3}{n}\right) = v_f\left(\frac{3}{n}-\frac{3}{m}\right) \Rightarrow d_{i-2}^\Delta$$
$$= \frac{l}{n} - (v_{i-2}^0 - v_{i-1}^0) = \frac{l}{n} - v_f\left(\frac{3}{n}-\frac{3}{m}-\frac{2}{n}+\frac{2}{m}\right)\cdot\Delta = \frac{l}{n} - v_f\cdot\left(\frac{1}{n}-\frac{1}{m}\right)\cdot\Delta = \frac{l}{m}$$

For vehicle $i-n+1$

$$d_{i-n+1}^0 = \frac{l}{n} \Rightarrow k_{i-n+1}^0 = \frac{n+\frac{m}{l}\left(l-\frac{nl}{n}\right)}{l} = \frac{n}{l} \Rightarrow v_{i-n+1}^0 = v_f\left(1-\frac{n}{m}\right) = v_f\left(\frac{n}{n}-\frac{n}{m}\right) \Rightarrow d_{i-n+1}^\Delta$$
$$= \frac{l}{n} - v_f\left(\frac{n}{n}-\frac{n}{m}-\frac{n-1}{n}+\frac{n-1}{m}\right)\cdot\Delta = \frac{l}{m}$$

However, the spacing between vehicle $i-n$ and $i-n+1$ remains the same as shown below.

$$d_{i-n}^0 = \frac{l}{n} \Rightarrow k_{i-n}^0 = \frac{n}{l} \Rightarrow v_{i-n}^0 = v_f\left(1-\frac{n}{m}\right) \Rightarrow d_{i-n}^{\Delta t} = \frac{l}{n} - v_f\left(1-\frac{n}{m}-\frac{n}{n}+\frac{n}{m}\right)\cdot\Delta = \frac{l}{n}$$
$$d_{i-n-1}^0 = \frac{l}{n} \Rightarrow k_{i-n-1}^0 = \frac{n}{l} \Rightarrow v_{i-n-1}^0 = v_f\left(1-\frac{n}{m}\right) \Rightarrow d_{i-n}^\Delta = \frac{l}{n} - v_f\left(1-\frac{n}{m}-1+\frac{n}{m}\right)\cdot\Delta = \frac{l}{n}$$

The above derivations show that vehicles i to $i-n+1$ (a total of n vehicles) change their spacing with their immediate lead vehicle to l/m. All the vehicles behind vehicle $i-n-1$ do not have spacing reduction. At time $t=0$, the shockwave is located at the back of vehicle $i+1$. After the clock tick, the location of the shockwave propagates to the back of vehicle $i-n+1$. This means that the shockwave travels n vehicles. As compared to the ground, the total change in distance can be expressed as $-n\cdot\frac{l}{m}$. Recall that $l = v_f\cdot\Delta$; it is can be seen that $\bar{\omega}_{12} = -\frac{n}{m}\cdot v_f$.

Checking with Eq. (21) it is apparent that $\omega_{12} = \bar{\omega}_{12}$. Q.E.D.

References

Balakrishna, R., 2006. Off-Line Calibration of Dynamic Traffic Assignment Models. Doctoral Dissertation, Massachusetts Institute of Technology.

Balakrishna, R., Koutsopoulos, H.N., Ben-Akiva, M., 2005. Calibration and validation of dynamic traffic assignment systems. In Mahmassani, H.S. (Eds.), Proceedings of the 16th International Symposium on Transportation and Traffic Theory, College Park, Maryland, pp. 407–426.

Ben-Akiva, M., 2003a. Development of a Deployable Real-time Dynamic Traffic Assignment System. Evaluation Report (Part A): Evaluation of Estimation and Prediction Capabilities. Massachusetts Institute of Technology.

Ben-Akiva, M., 2003b. Development of a Deployable Real-time Dynamic Traffic Assignment System. Evaluation Report (Part B): Planning Functionality (DynaMIT-P) and Applications. Massachusetts Institute of Technology.

Ben-Akiva, M., Bierlaire, M., Burton, D., Koutsopoulos, H.N., Mishalani, R., 2001. Network state estimation and prediction for real-time traffic management. Networks and Spatial Economics 1 (3–4), 293–318.

Ben-Akiva, M., Bierlaire, M., Koutsopoulos, H.N., Mishalani, R., 1998. DynaMIT: A Simulation-based System for Traffic Prediction. Presented at the DACCORD Short Term Forecasting Workshop, Delft, The Netherlands.

Ben-Akiva, M., Cuneo, D., Hasan, M., Jha, M., Yang, Q., 2003. Evaluation of freeway control using a microscopic simulation laboratory. Transportation Research Part C 11 (1), 29–50.

Ben-Akiva, M.E., Darda, D., Jha, M., Koutsopoulos, H.N., Toledo, T., 2004. Calibration of microscopic traffic simulation models with aggregate data. In: Proceedings of the 83rd Annual Meeting of Transportation Research Board, Washington DC, USA.

Botma, H., 1978. State-of-the-art Traffic Flow Models. Research Report R-78-40, SWOV.

Boyles, S., Ukkusuri, S., Waller, T., Kockelman, K., 2005. A Comparison of static and dynamic traffic assignment under tolls in the Dallas–Fort Worth region. In: Proceedings of the 84th Annual Meeting of Transportation Research Board, Washington, DC, USA.

Branston, D., 1976. Models of single lane time headway distributions. Transportation Science 10 (2), 125–148.
Buckley, D.J., 1968. A semi-Poisson model of traffic flow. Transportation Science 2 (2), 107–132.
Burghout, W., 2004. Hybrid Microscopic–Mesoscopic Traffic Simulation. Doctoral Dissertation, Royal Institute of Technology.
Celikoglu, H.B., Dell'Orco, M., 2007. Mesoscopic simulation of a dynamic link loading process. Transportation Research Part C 15 (5), 329–344.
Cetin, N., Burri, A., Nagel, K., 2003. A Large-scale agent-based traffic microsimulation based on queue model. In: Proceedings of the 3rd swiss transport research conference, Monte Verita, Ascona.
Chiu, Y.-C., Zheng, H., 2007. Real-time mobilization decisions for multi-priority emergency response resources and evacuation flows: model formulation and solution. Transportation Research Part E 43 (6), 710–736.
Chiu, Y.-C., Zheng, H., Villalobos, J.A., Gautam, B., 2007. Modeling no-notice mass evacuation using a dynamic traffic flow optimization model. IIE Transactions 39 (1), 83–94.
Daganzo, C.F., 1994. The cell transmission model: a dynamic representation of highway traffic consistent with the hydrodynamic theory. Transportation Research Part B 28 (4), 269–287.
Daganzo, C.F., 1995a. The cell transmission model, part II: network traffic. Transportation Research Part B 29 (2), 79–93.
Daganzo, C.F., 1995b. Requiem for second-order fluid approximations of traffic flow. Transportation Research Part B 29 (4), 277–286.
Dell'Orco, M., 2006. A dynamic network loading model for mesosimulation in transportation systems. European Journal of Operational Research 175 (3), 1447–1454.
FHWA, 2007. Traffic Analysis Toolbox Volume IV: Guidelines for Applying CORSIM Microsimulation Modeling Software. McLean, VA, Office of Operations.
Gawron, C., 1998. An iterative algorithm to determine the dynamic user equilibrium in a traffic simulation model. International Journal of Modern Physics C 9 (3), 393–407.
Ge, Y.E., Carey, M., 2004. Travel time computation of link and path flows and first-in–first-out. In: Proceedings of the 4th International Conference on Traffic and Transportation Studies, Dalian, China, Beijing.
INRO., 2005. DYNAMEQ, <http://www.inro.ca/en/products/dynameq/index.php>.
Jayakrishnan, R., Mahmassani, H.S., Hu, T.-Y., 1994. An evaluation tool for advanced traffic information and management systems in urban networks. Transportation Research Part C 2 (3), 129–147.
Jin, W., 2003. Kinematic Wave Models of Network Vehicular Traffic. Doctoral Dissertation, University of California, Davis.
Lenz, H., Wagner, C.K., Sollacher, R., 1999. Multi-anticipative car-following model. European Physical Journal B 7 (2), 331–335.
Leonard, D.R., Power, P., Taylor, N.B., 1989. CONTRAM: Structure of the Model. Transportation Research Laboratory, Crowthorn.
Li, Y., Ziliaskopoulos, A.K., Waller, S.T., 1999. Linear programming formulations for system optimum dynamic traffic assignment with arrival time-based and departure time-based demands. Transportation Research Record 1667, 52–59.
Lighthill, M.J. Whitham, G.B., 1955. On kinematic waves: II. A theory of traffic flow in long crowded roads. In: Proceedings of Royal Society of London, Series A. Mathematical and Physical Sciences.
Mahmassani, H.S., 2001. Dynamic network traffic assignment and simulation methodology for advanced system management applications. Networks and Spatial Economics 1 (3–4), 267–292.
Mahmassani, H.S., Peeta, S., Hu, T.-Y., Ziliaskopoulos, A.K., 1993. Dynamic traffic assignment with multiple user classes for real-time ATIS/ATMS applications. In: Proceedings of the ATMS Conference on Management of Large Urban Traffic Systems, St. Petersburg, FL, USA, pp. 91–114.
Mahmassani, H.S., Sbayti, H., Victoria, I., Zhou, X., Chiu, Y.-C., 2003. TrEPS-P, Phase 1.5C, Final Report Volume 1 – DYNASMART Calibration and Evaluation. College Park, MD, Maryland Transportation Initiative.
Mahut, M., 2001. A Discrete Flow Model for Dynamic Network Loading. Doctoral Dissertation, University of Montreal.
Mahut, M., Florian, M., Tremblay, N., 2002. Application of a simulation-based dynamic traffic assignment model. In: Proceedings of the 5th IEEE International Conference on Intelligent Transportation Systems, Singapore.
Mahut, M., Florian, M., Tremblay, N., Campbell, M., Patman, D., McDaniel, Z.K., 2004. Calibration and application of a simulation-based dynamic traffic assignment model. Transportation Research Record 1876, 101–111.
Nelson, P., Sopasakis, A., 1998. The Prigogine–Herman kinetic model predicts widely scattered traffic flow data at high concentrations. Transportation Research Part B 32 (8), 589–604.
Newell, G.F., 1993. A simplified theory of kinematic waves in highway traffic, part I: general theory. Transportation Research Part B 27 (4), 281–287.
NGSIM., 2005. <http://www.ngsim.fhwa.dot.gov/>.
Peeta, S., Ziliaskopoulos, A.K., 2001. Foundations of dynamic traffic assignment: the past, the present and the future. Networks and Spatial Economics 1 (3–4), 233–265.
PTV., 2009. VISSIM Website <http://www.ptvamerica.com/main.html>.
Richards, P.I., 1956. Shockwaves on the highway. Operations Research 4 (1), 42–51.
Taylor, N.B., 2003. The CONTRAM dynamic traffic assignment model. Networks and Spatial Economics 3 (3), 297–322.
Waller, S.T., Schofer, J.L., Ziliaskopoulos, A.K., 2001. Evaluation with traffic assignment under demand uncertainty. In: Proceedings of the 80th Annual Meeting of Transportation Research Board, Washington, DC, USA.
Zhang, H.M., 2001. New perspectives on continuum traffic flow models. Networks and Spatial Economics 1 (1–2), 9–33.
Ziliaskopoulos, A.K., Lee, S., 1997. A cell transmission based assignment-simulation model for integrated freeway/surface street systems. In: Proceedings of the 76th Annual Meeting of the Transportation Research Board, Washington, DC, USA.
Ziliaskopoulos, A.K., Waller, S.T., 2001. A dynamic and stochastic approach to network design. Transportation Research Record 1771, 106–114.